Mineralium Deposita (2022) 57:319–342
https://doi.org/10.1007/s00126-021-01064-1

ARTICLE

Geology and geochemistry of the Tulaergen conduit-style magmatic Ni-Cu sulfide deposit in the Central Asian Orogenic Belt, northwestern China

Yalei Wang[1,2] · Chusi Li[3] · Wenyuan Li[1] · Zhaowei Zhang[1] · Edward M. Ripley[3] · Yongbao Gao[1] · Jiangwei Zhang[1]

Received: 12 November 2020 / Accepted: 9 June 2021 / Published online: 14 August 2021

Abstract

The Tulaergen magmatic Ni-Cu sulfide ore deposit is located along the southern margin of the Central Asian Orogenic Belt in northwestern China. This deposit is hosted by a small mafic–ultramafic complex composed of a Late Carboniferous (~ 301 Ma) gabbroic member at the margin and a younger ultramafic dyke in the center. Net-textured and semi-massive sulfides are mainly concentrated in the steeply dipping, widened parts of the dyke. Zircons from the ultramafic member yield a U–Pb age of 281 ± 2 Ma, ~ 20 myr younger than the gabbroic member. The average $\varepsilon_{Hf}(t)$ value of the zircons is ~ 16. The Tulaergen mafic–ultramafic rocks are characterized by light REE enrichments, pronounced negative Nb–Ta anomalies, $(^{87}Sr/^{86}Sr)_i$ ratios from 0.7034 to 0.7036, and $\varepsilon_{Nd}(t)$ values from 5.1 to 6.9. The isotope data indicate negligible bulk contamination with the crust. The $\delta^{34}S$ values of sulfide ores are from − 0.3 to 1.5‰, similar to the values of the country rocks. The γ_{Os} values of the sulfide ores are from + 605 to + 954, much higher than typical mantle values. The Os-S isotope data together support the view that the addition of Os-bearing organic matter from the country rocks may have played a critical role in triggering sulfide saturation. In the sub-vertical segment of the deposit, the upper zone has lower PGE tenors coupled with lower and rather constant olivine Fo contents compared to the lower zone. Based on the geometry of the dyke and sulfide distribution, we conclude that the Tulaergen deposit formed in a dynamic magma conduit.

Keywords Magmatic sulfide deposits · Mafic–ultramafic rocks · Magma conduit · Sr-Nd-Hf-S-Os isotopes · PGE geochemistry

Introduction

Numerous mafic–ultramafic intrusions are present in East Tianshan, which is located at the southern margin of the Central Asian Orogenic Belt in northern Xinjiang, western China (Fig. 1). A few of these intrusions were emplaced between 313 and 479 Ma (zircon U–Pb ages, Xie et al. 2012; Su et al. 2014). One of these intrusions, namely the Heishan intrusion, contains low grade (0.6 wt% Ni) sulfide mineralization (Xie et al. 2014). The majority of mafic–ultramafic intrusions in the region formed in the Early-Middle Permian, with magmatic zircon U–Pb ages varying from 288 to 266 Ma (see summary in Xue et al. 2016a; Song et al., 2021). Some of these intrusions host economically valuable magmatic Ni-Cu sulfide ore deposits, such as Huangshanxi (Mao et al. 2014), Huangshandong (Mao et al. 2015), and Tulaergen (San et al. 2010). The formation of these deposits has been linked to the Tarim mantle plume (Pirajno et al. 2008; Qin et al. 2011; Zhang and Zou 2013), to subduction-related magmatism (Xiao et al. 2004), or to magmatism associated with lithospheric delamination coupled with asthenosphere upwelling in a post-subduction environment (Song et al. 2013, 2021; Li et al. 2019). Central to the debate of these different models are the different views on the timing of the final

Communicated by Editorial handling: W. D. Maier.

✉ Chusi Li
cli@indiana.edu

[1] MNR Key Laboratory for the Study of Focused Magmatism and Giant Ore Deposits, Xi'an Center of China Geological Survey, Xi'an 710054, China

[2] Institute of Mineral Resources, Chinese Academy of Geological Science, Beijing 100037, China

[3] Department of Earth and Atmospheric Sciences, Indiana University, Bloomington, IN 47405, USA

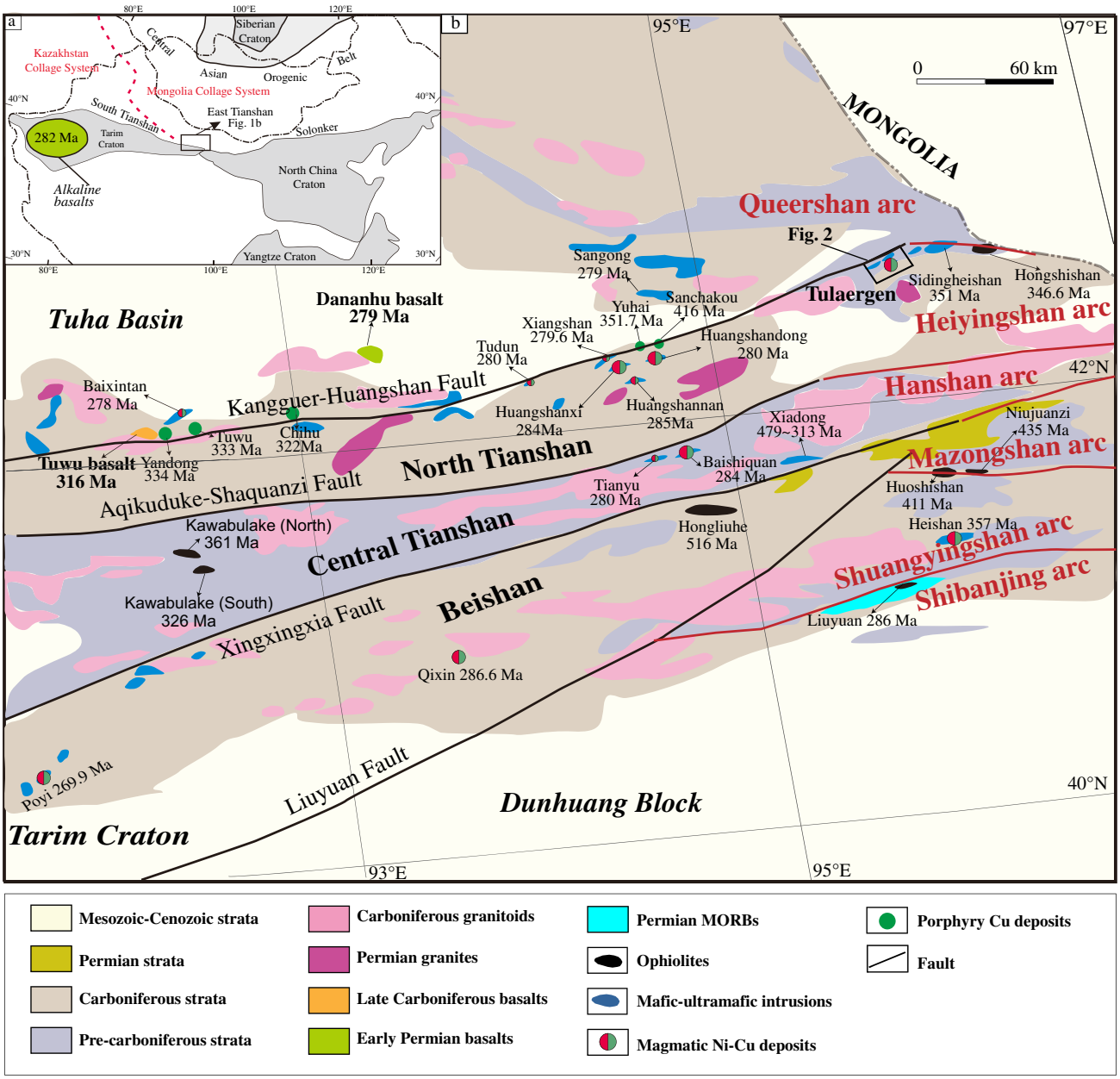

Fig. 1 **a** Outline of the Central Asian Orogenic Belt (modified from Jahn 2004 and Xiao et al. 2015). **b** Simplified geological map of the East Tianshan–Beishan Orogenic Collage (modified from Xiao et al. 2019, age data from Table S1)

episode of subduction and arc-continent collision in East Tianshan, which varies from the end of the Carboniferous (e.g., Han and Zhao 2018) to the Early Triassic (e.g., Xiao et al. 2004). Existing geological data, such as the ages of ophiolites, blueshists, eclogites, marine sedimentary rocks, arc volcanic rocks, and stitching plutons (granite intrusions across a collision zone) in East Tianshan do not discount either of these models. The proponents of the younger age for the tectonic transition partly base their interpretation on the classification of the Permian mafic–ultramafic intrusions in the region as Alaskan-type complexes (e.g., Xiao et al. 2004, 2019). The proponents of the older age for the tectonic transition in East Tianshan mainly rely on several lines of evidence from West Tianshan, such as the occurrence of 316 Ma stitching plutons (Han et al. 2010) and the 305–312 Ma eclogites (Klemd et al. 2011; Li et al. 2016). Based on regional geology, plus the presence of Early Permian MORB-like basalts in the Liuyuan ophiolite belt (Mao et al. 2012) and several Triassic stitching

plutons across the suture zones (Li et al. 2012a) in the East Tianshan–Beishan Orogenic Collage, Xiao et al. (2010, 2019) proposed that this segment of the Paleo-Asian Ocean was completely consumed at the end of the Middle Permian, implying that all of the Early Permian magmatic Ni-Cu sulfide deposits in the region are subduction-related.

We have selected the Tulaergen deposit to test the above-mentioned hypotheses. We use new zircon U–Pb age data to determine if there is a significant age gap between the sulfide-mineralized ultramafic body and the associated gabbros, a common feature of arc mafic–ultramafic complexes in southern Alaska (e.g., Thakurta et al. 2008). New mineralogical and geochemical data (incompatible trace elements, platinum-group elements, and Sr–Nd-Hf-Os-S isotopes) are used to assess if the Tulaergen igneous complex are consistent with the mafic–ultramafic intrusive rocks having formed from arc basalts. Finally, we use these data to evaluate the fundamental controls on the sulfide mineralization in this complex, which remain poorly understood in spite of several previous studies (San et al. 2010; Jiao et al. 2012; Tang et al. 2012; Zhao et al. 2017; Wang et al. 2018).

There is no previous age data for the ultramafic member of the Tulaergen mafic–ultramafic complex. San et al. (2010) reported a zircon U–Pb age of 300.5 ± 3.2 Ma for the gabbroic member of this complex. Based on this age, these authors suggested that the deposit formed in a collisional tectonic setting, despite the fact that the rocks show arc-like trace element characteristics, such as pronounced negative Nb–Ta anomalies and light REE enrichments. Jiao et al. (2012) used the observed similar mantle-normalized incompatible trace element patterns between the gabbroic and ultramafic members as evidence for a common parental magma. These authors also reported low PGE tenors of the sulfide ores and attributed this phenomenon to sulfide retention in the mantle source. Tang et al. (2012) proposed a two-stage crustal contamination model, and the addition of crustal S appears may be the key factors controlling sulfide saturation and sulfide segregation based on the Sr–Nd-Os-S isotope data. Zhao et al. (2017) reported Cu isotope variation between different types of sulfide mineralization and attributed such variation to sulfide-magma differentiation on cooling. Wang et al. (2018) reported similar trace element ratios, Sr–Nd isotopes and PGE compositions between the mafic enclaves and the ultramafic host rocks. Based on such similarities, plus abundant hydrous silicate minerals in some mafic enclaves, they suggested a model of liquid immiscibility to explain the coexistence of mafic and ultramafic rocks, and attributed such a process to high water content in the mantle-derived magma. They speculated that the assumed original high water content in the magma was due to previous subduction modification of the mantle source.

Geological background

Regional geology

The Central Asian Orogenic Belt (CAOB) is bounded by the Siberian craton to the north and by the Tarim and North China cratons to the south (Fig. 1a). The CAOB is sub-divided into the Mongolia Collage System in the east and the Kazakhstan Collage System in the west (Xiao et al. 2010, 2015, 2019). According to these authors, the East Tianshan–Beishan Orogenic Collage is the southwestern member of the Mongolia Collage System.

East Tianshan is the western part of the East Tianshan–Beishan Orogenic Collage, and is traditionally further divided into two fault-bounded sub-terranes, namely Central Tianshan in the south and North Tianshan in the north (Fig. 1b). The Central Tianshan terrane is geologically the western extension of the Hanshan arc terrane (Xiao et al. 2010, 2019). Both terranes are largely composed of high-grade metamorphic rocks that have undergone high-T but low-P metamorphism, with unknown metamorphic age (Liu and Wang 1995), and intrusion of Carboniferous-Triassic granitoids (Nie et al. 2002). These terranes are bounded to the south by the Beishan terrane (Fig. 1b), which in turn is bounded by the Tarim Craton to the southwest and by the Dunhuang Block to the southeast (Xiao et al. 2010, 2019).

The Dunhuang Block is composed of Neoarchean tonalite-trondhjemite-granodiorite gneisses, and Proterozoic granitoids and metamorphosed supracrustal rocks (e.g., Lu et al. 2008). It is interpreted to be an active continental margin of the Tarim Craton in the Proterozoic by some researchers (e.g., Zhao and Cawood 2012). The boundary between the active continental margin and the accreted Hanshan arc terrane is marked by the Liuyuan ophiolite belt, which is composed of massive basalts, pillow basalts, basaltic breccia, gabbros and ultramafic rocks, associated with cherts and tuffs (Fig. 1b). The basalts and gabbros have MORB-like mantle-normalized trace element patterns and depleted Sr–Nd isotopes (Mao et al. 2012). Zircons from the gabbros yield a U–Pb age of ~ 286 Ma (Mao et al. 2012). Based on these data, Xiao et al. (2010, 2019) suggested that the Liuyuan Ocean, a branch of the Paleo-Asian Ocean was completely consumed by subduction after the Early Permian, possibly in the Middle Permian.

The North Tianshan terrane is bounded by the Tuha basin to the northwest and the Queershan terrane to the northeast (Fig. 1b). The Tuha basin is filled with Carboniferous-Permian volcanic-sedimentary rocks, and covered by Cenozoic sediments. The Queershan terrane is a volcanic arc terrane that was accreted in the Permian to the present-day southern margin of the Siberian Craton according to Xiao et al. (2010, 2019). This accreted arc terrane is mainly composed of Ordovician-Permian andesites, dacites, and rhyolites,

intercalated with greywackes, shales, and slates (Wang et al. 2004).

The North Tianshan terrane is the western extension of the Heiyingshan arc terrane according to Xiao et al. (2010, 2019). Both terranes are mainly composed of Carboniferous felsic volcanic rocks with arc-like trace element compositions, and carbonates and clastic sedimentary rocks including terrestrial clastic rocks that are intercalated with cherts, limestones, and volcanic rocks (Liu and Wang 1995). The Queershan and Heiyingshan arc terranes are separated by the Hongshishan ophiolite belt (Fig. 1b). Zircons from gabbro of this ophiolite belt yield a U–Pb age of 346.6 Ma (Zuo et al. 1990). The Hongshishan ophiolites are regarded as the remnants of the Paleo-Asian Ocean that was completely consumed at the end of Early Permian by subduction (Xiao et al. 2010, 2019).

The Xingxingxia–Shibanjing ophiolite belt between the North Tianshan–Mazongshan and Hanshan–Central Tianshan arc terranes is composed of ultramafic rocks, gabbros, basalts and clastic rocks in a turbidite matrix containing Ordovician and Silurian fossils (Zuo et al. 1990, 1991; Nie et al. 2002). Zircons from the gabbros of the ophiolite complexes yield U–Pb ages from 350 to 321 Ma. Based on the age data and geology, Xiao et al. (2010, 2019) suggested that this ophiolite belt resulted from the closure of a branch of the Paleo-Asian Ocean at the end of the Silurian by subduction.

In summary, the East Tianshan–Beishan Orogenic Collage consists of several subparallel E–W trending arc terranes that were amalgamated together by protracted subduction processes that lasted until the end of the Early Permian in the northern part and until the end of the Middle Permian in the southern part according to Xiao et al. (2010, 2019).

Protracted magmatism and associated mineral deposits

Similar to other orogenic belts worldwide, the East Tianshan–Beishan Orogenic Collage is characterized by widespread, abundant granitoids (Fig. 1b). The zircon U–Pb ages of the dated granitoids in this orogenic collage vary from 462 to 230 Ma (Zhou et al. 2010 and reference therein), with two age peaks, one at ~ 440 Ma and another at ~ 280 Ma (Fig. 2a). The older age peak is 26 myr younger than the only known eclogite (466 Ma; Saktura et al. 2017) in the region; the younger age peak is similar to the youngest ages of basalts (excluding MORBs of ophiolite complexes) and andesites in the region (Fig. 2a; Liu et al. 2016). The younger (Permian) episode of granitic magmatism is mainly restricted to North Tianshan, whereas the older (Carboniferous) episode of granitic magmatism is more widespread (Fig. 1b). The zircon U–Pb ages of gabbros in the ophiolite complexes of the East Tianshan–Beishan Orogenic Collage vary from 516 to 286 Ma (Fig. 2a).

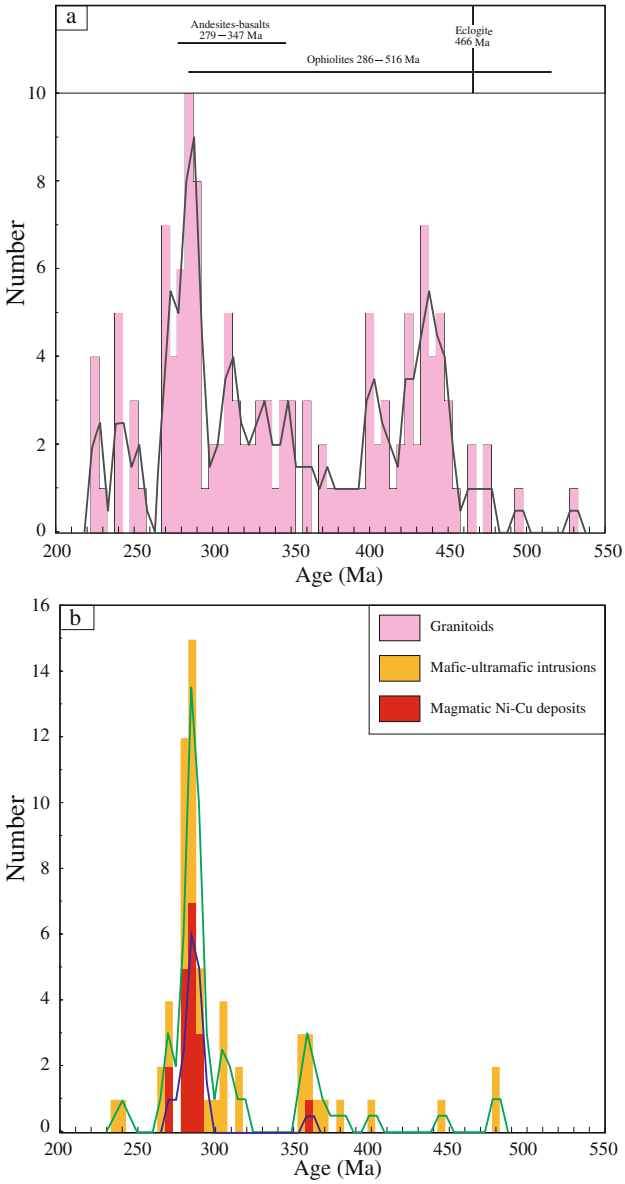

Fig. 2 Age distributions of granitoids, andesites-basalts, ophiolites, eclogite, and mafic–ultramafic intrusions and associated Ni-Cu sulfide deposits in the East Tianshan–Beishan Orogenic Collage (data from Table S1)

Several porphyry Cu ± Mo deposits associated with granitoids are present in the region, mainly in North Tianshan (Fig. 1b). These include the Tuwu, Yandong, Chihu, Yuhai, and Sanchakou deposits. The zircon U–Pb ages of the host rocks and the molybdenite Re-Os ages of the ores are between 416 and 322 Ma (Fig. 1b; Wang et al. 2016, 2017).

Mafic–ultramafic intrusions are widespread in the East Tianshan–Beishan Orogenic Collage (Fig. 1b). The zircon U–Pb ages of the dated intrusions are from 479 to 233 Ma (Xue et al. 2016a; Song et al., 2021), with a peak at ~ 280 Ma, similar to the younger age peak of granitoids

in the region (Table S1, Fig. 2a, b). The oldest known magmatic Ni-Cu sulfide deposit, i.e., the Heishan deposit, has a zircon U–Pb age of 357 Ma (Fig. 1b and 2b; Xie et al. 2012). The other known magmatic Ni-Cu sulfide deposits in the region formed between 287 and 269 Ma, with most of them between 285 and 280 Ma (Fig. 1b and 2b; Qin et al. 2011; Xue et al. 2016a, b; Song et al., 2021).

The Tulaergen sulfide-mineralized mafic–ultramafic complex

The Tulaergen mafic–ultramafic complex, which hosts a major magmatic Ni-Cu sulfide deposit, is located in the easternmost part of North Tianshan (Fig. 1b). This complex was referred to as the No. I mafic–ultramafic intrusion previously (San et al. 2010; Jiao et al. 2012; Zhao et al. 2017; Wang et al. 2018). Two older gabbroic intrusions without significant sulfide mineralization, namely the No. II and III mafic intrusions are present several hundred meters to the north and to the west, respectively (Fig. 3a). The gabbroic intrusions are spatially associated with the Kangguer-Huangshan fault (Fig. 3a), which controls the distribution of several mafic–ultramafic intrusions in the region (Fig. 1b; Xiao et al. 2010, 2019). The country rocks of the No. I mafic–ultramafic complex and the nearby gabbroic intrusions (No. II, III) are Middle-Late Carboniferous volcanic-sedimentary rocks, plus undated diorites and granites (Fig. 3a, b). The zircon U–Pb age data show that the No. II intrusion was emplaced at ~ 357 Ma and the No. III intrusion plus the mafic member of the No. I mafic–ultramafic complex were emplaced at ~ 351 Ma (San et al. 2010; Jiao et al. 2013).

The surface-exposed area of the Tulaergen sulfide-mineralized mafic–ultramafic complex is ~ 740 m long and 30 ~ 50 m wide, with downward extension from ~ 10 to ~ 300 m (Fig. 3b, c). The western part of this intrusive complex is located 80–400 m beneath the Middle-Late Carboniferous volcanic-sedimentary rocks. The deepest downward extension of this part is ~ 600 m below the surface (Fig. 3c). The unexposed part is volumetrically larger than the exposed one.

Based on the change in geometry, the Tulaergen intrusive complex can be divided into three segments: the eastern, middle, and western segments (Fig. 3b, d). The long section (Fig. 3d) is drawn using drill core data, projected horizontally to a central plane from point A to A' (Fig. 3b). As shown by the cross-sections (Fig. 3c) and the long section (Fig. 3d), the Tulaergen intrusive complex is a tilted-elongated S-shaped dyke-like body, with an overall southeast dip and southwest plunge (Fig. 3c, d). Dip and plunge are very gentle in the eastern segment. The western segment is almost flat lying. The middle segment is characterized by sub-vertical dip and plunge. This segment can be further divided into a lower widened part and an upper widened part connected by a thin neck. Sulfide ores are more abundant in the widened parts than in the neck (Fig. 3c).

Lithologically, the Tulaergen intrusive complex consists of an older (301 Ma; San et al. 2010) gabbroic intrusion and a younger ultramafic dyke (281 Ma; this study) (Fig. 3b–d). The gabbroic rocks are mainly present at the margin of the complex, but some large blocks together with large fragments of volcanic-sedimentary country rocks also occur in the lower part of the middle segment of the complex (Fig. 3c, d). Small xenoliths of gabbroic rocks and volcanic-sedimentary country rocks are widespread in the ultramafic dyke (Wang et al. 2018).

The Tulaergen ultramafic dyke is almost entirely sulfide-mineralized, containing visible base metal sulfides (pyrrhotite, pentlandite, and chalcopyrite). The deposit contains 20 million metric tons of sulfide ores with average grades of 0.6 wt% Ni and 0.4 wt% Cu (Jiao et al. 2012). Massive and net-textured sulfides mainly occur in the middle segment of the dyke (Fig. 3d). The mine data indicate that the sulfide ores in this segment account for ~ 80% of the total reserve of the deposit. No massive sulfides are found in the western segment. A small massive sulfide zone is present at the base of the eastern segment, overlain by disseminated sulfides (Fig. 3d). There are two large massive sulfide orebodies in the middle segment, one in the lower part and the other in the upper part of this segment (Fig. 3c). Each of them is surrounded by net-textured sulfides or disseminated sulfides (Fig. 3d). In cross-sections (Fig. 3c), the massive sulfide orebodies are sub-vertical, subparallel to the walls of the ultramafic member, and closer to the southeast wall than the northwest wall. The distribution of different types of sulfide ores in this segment is generally similar to that in the steeply-dipping western segment of the Jinchuan intrusion (see Fig. 1 of Li et al. 2004) and in the feeder dyke (the Mini Ovoid) of the Voisey's Bay intrusion (see Fig. 9 of Li and Naldrett 1999).

Sample description

A large plagioclase-bearing, sulfide-poor lherzolite sample (~ 10 kg) for zircon separation and U–Pb age determination was collected from an underground mining tunnel in the middle segment of the deposit (Fig. 3b), at a depth of ~ 200 m below surface (Fig. 3d). The other samples were collected from two drill cores (ZK 1106, ZK1501) in the middle segment (Fig. 3b, d) and the same underground mining tunnel at the same depth as the sample for dating, and from another drill core (ZK3302) located in the western segment (Fig. 3b). The samples encompass all major rock types of the complex and all major types of sulfide ores of the deposit.

Based on the IUGS-recommended classification, the ultramafic dyke of the Tulaergen intrusive complex is

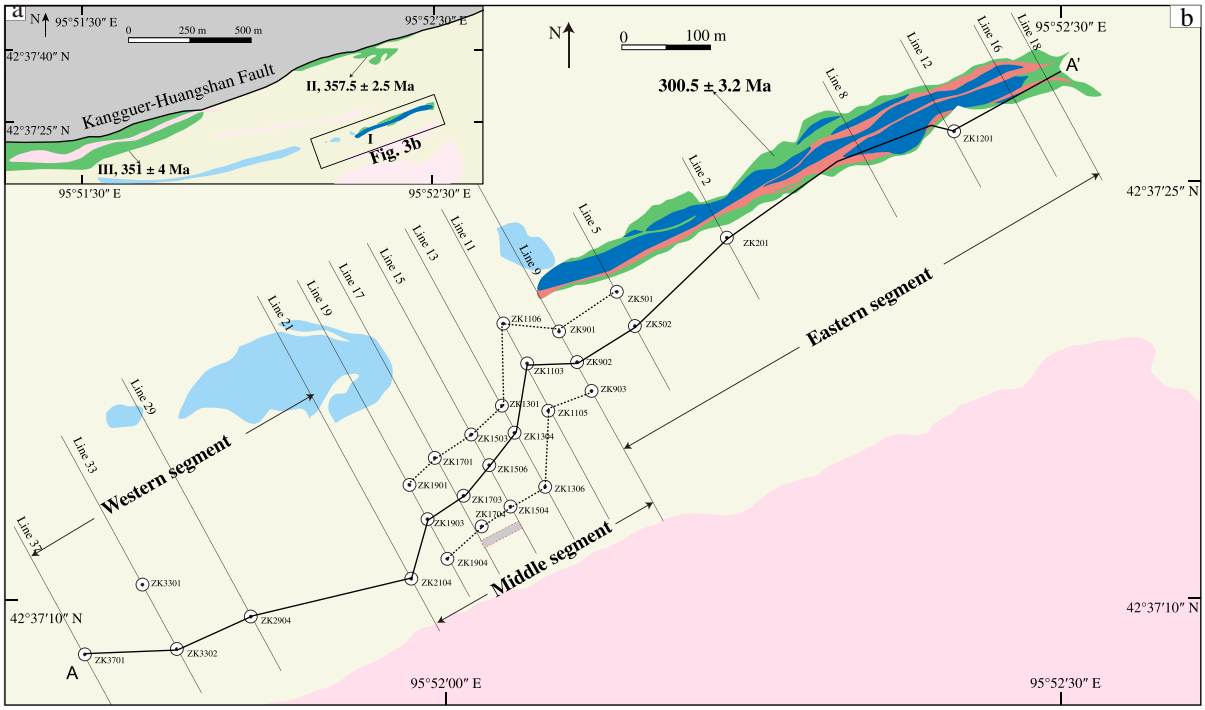
a
95°51′30″ E
95°52′30″ E
42°37′40″ N
42°37′25″ N
0 250 m 500 m
Kangguer-Huangshan Fault
II, 357.5 ± 2.5 Ma
III, 351 ± 4 Ma
Fig. 3b
b
N
0 100 m
300.5 ± 3.2 Ma
A'
A
Eastern segment
Western segment
Middle segment
42°37′25″ N
42°37′10″ N
95°52′00″ E
Line 2
Line 5
Line 8
Line 9
Line 11
Line 12
Line 13
Line 15
Line 16
Line 17
Line 18
Line 19
Line 21
Line 29
Line 31
Line 33
ZK201
ZK501
ZK502
ZK901
ZK902
ZK903
ZK1103
ZK1105
ZK1106
ZK1201
ZK1301
ZK1306
ZK1503
ZK1504
ZK1506
ZK1701
ZK1703
ZK1704
ZK1901
ZK1903
ZK1904
ZK2104
ZK2904
ZK3301
ZK3302
ZK3701

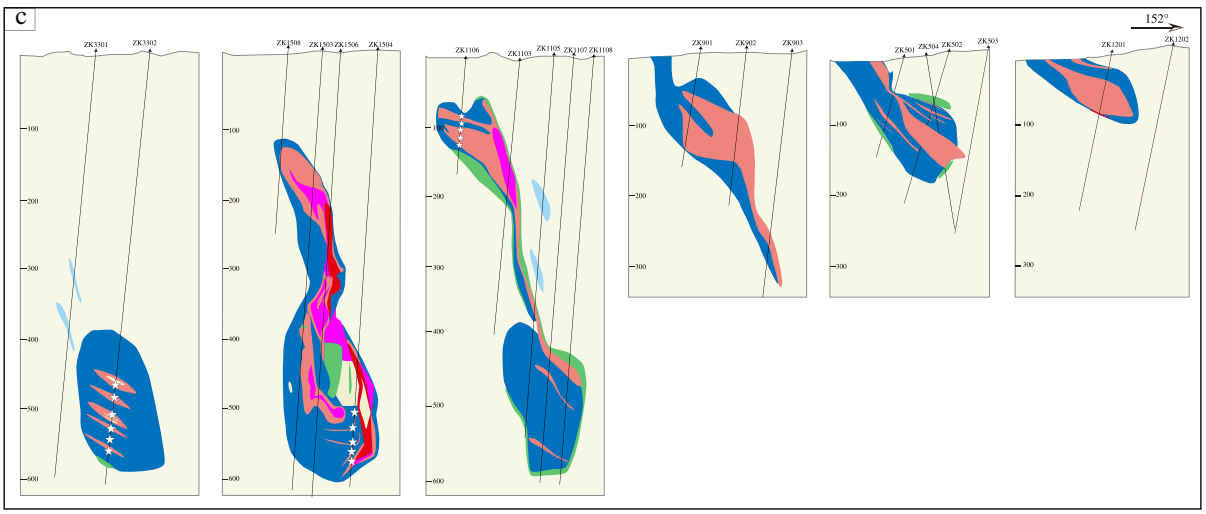
c
152°
ZK3301
ZK3302
ZK1508
ZK1503
ZK1506
ZK1504
ZK1106
ZK1103
ZK1105
ZK1107
ZK1108
ZK901
ZK902
ZK903
ZK501
ZK504
ZK502
ZK503
ZK1201
ZK1202

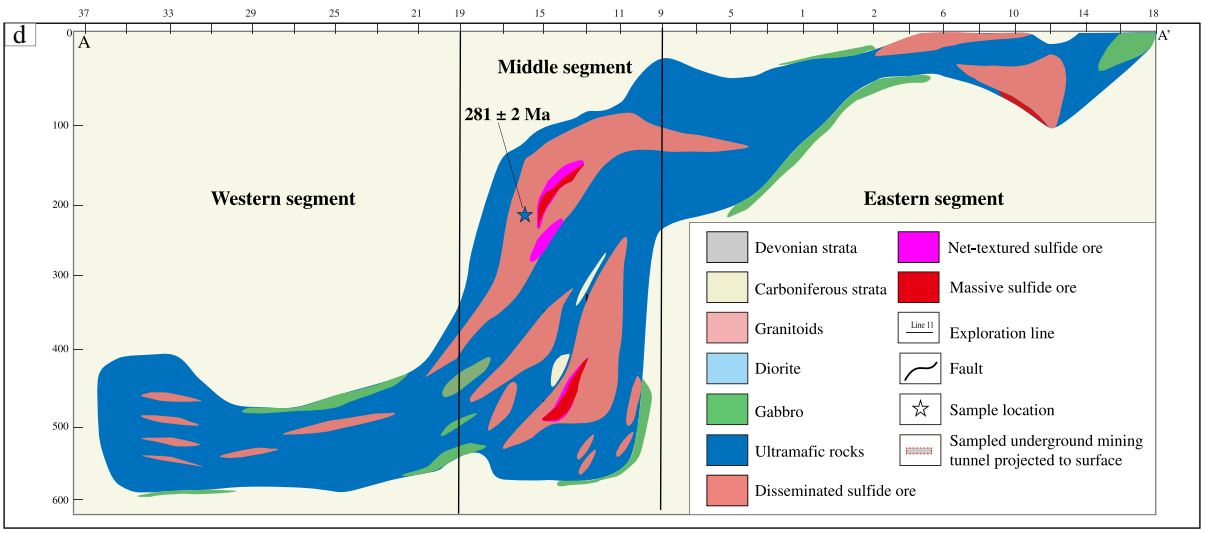
d
A
A'
Middle segment
281 ± 2 Ma
Western segment
Eastern segment
Devonian strata
Carboniferous strata
Granitoids
Diorite
Gabbro
Ultramafic rocks
Disseminated sulfide ore
Net-textured sulfide ore
Massive sulfide ore
Exploration line
Fault
Sample location
Sampled underground mining tunnel projected to surface

◂**Fig. 3** **a** A simplified geological map of the Tulaergen area. **b** A plan view of the Tulaergen mafic–ultramafic complex. **c** Cross-sections of the Tulaergen magmatic sulfide deposit. **d** A long section of the deposit by horizontal projection of drill core data from both sides to a central plane from A to A' (data are from the 2016 internal report of the Sixth Geological Team of the Xinjiang Bureau of Geological and Mineral Resources)

predominantly composed of lherzolite, plus a minor amount of olivine websterite. The lherzolite samples contain 50–70% (in volume) olivine, 10–20% orthopyroxene, and 10–15% clinopyroxene, with minor plagioclase and hornblende (Fig. 4a, b). Olivine is a cumulus phase, and the other silicate minerals occur in the interstitial spaces. Some pyroxene crystals occur as oikocrysts enclosing small grains of olivine. The olivine websterite samples contain 30–40% olivine, 30–40% orthopyroxene, and 20–30% clinopyroxene, plus small amounts of plagioclase and hornblende (Fig. 4c). Some pyroxenes occur as large oikocrysts enclosing small olivine grains, and plagioclase and hornblende occur in the interstitial spaces. Based on the textures and the nomenclature of Irvine (1982), the ultramafic rocks are mainly orthocumulates.

The gabbro of the complex, which is ~ 20 myr older than the ultramafic dyke, is composed of 60–75% plagioclase and 20–30% clinopyroxene, with minor amounts of hornblende and biotite (Fig. 4d). Large plagioclase crystals are partially orientated and well packed, forming a framework. Small hornblende and biotite crystals occur inside the plagioclase frameworks. The texture indicates that this rock is a plagioclase mesocumulate (Irvine 1982).

Net-textured sulfide mineralization is mainly associated with lherzolite (Fig. 4e, f). Olivine in the sulfide-rich samples (Fig. 4e, f) is generally more severely altered to serpentine plus secondary magnetite than in the sulfide-poor samples (Fig. 4a–c).

Analytical methods

Zircon U–Pb isotope analysis was performed using a Neptune ICP-MS instrument equipped with a New Wave 193 nm-FX ArF excimer laser-ablation sampling system in the MLR Key Laboratory for the Study of Focused Magmatism and Giant Ore Deposits, Xi'an Center of China Geological Survey, Xi'an, China. The 91,500 zircon standard with the U-Th-Pb isotope ratios recommended by Wiedenbeck et al. (1995) and the Hf isotope ratio given by Machado and Simonetti (2001) were used for calibration. The Plesovice zircon standard (337.13 ± 0.37 Ma, Sláma et al. 2008) was used as a reference. The NIST SRM610 glass standard was used as an external standard to calculate the U, Th, and Pb concentrations in zircon. Data reduction was performed using the ICP-MS DataCal10.8 program. Plotting and age calculations were done using the Isoplot/Ex3.75 software of Ludwig (2012).

Mineral compositions were determined by wavelength dispersive X-ray analysis using a CAMECA SX50 electron microprobe at Indiana University. The analytical conditions for major and minor elements were 15 kV, 20 nA beam current, 1 μm beam size, and peak-counting time of 20 s. Nickel and Ca in olivine were analyzed using a beam current of 100 nA and a peak-counting time of 50 s. The detection limits for Ni and Ca under such conditions are 100 ppm and 50 ppm, respectively.

Whole-rock major element compositions were determined by X-ray fluorescence using a ZSX Primus II machine in the laboratory of the Wuhan Sample Solution Analytical Technology Ltd. Four standards (GBW07102, GBW07105, GBW07111, and GBW07112) were used to monitor data quality. Whole-rock trace element concentrations were determined using an Agilent 7700e ICP-MS in the same laboratory. The rock powder (~ 50 mg) was dissolved in a Teflon bomb using a mixture of HF and HNO_3. The Teflon bomb was put in a stainless-steel pressure jacket and heated to 190 °C in an oven for > 24 h. After cooling, the Teflon bomb was opened and placed on a hotplate at 140 °C and evaporated to dryness. The dried sample was refluxed with 1 ml of HNO_3. The final solution was diluted to ~ 100 g with 2% HNO_3 in a polyethylene bottle. Four standards (AGV-2, BHBO-2, BCR-2, and RGM-2) were used to monitor data quality. The duplicate analyses of these standards yield analytical errors of ± 5% for most trace elements.

Whole-rock Sr–Nd isotopes were measured using a Nu plasma HR MC-ICP-MS in the State Key Laboratory of Continental Dynamics, Northwest University, Xi'an, China. The total procedural blanks contain 0.04 ppb Rb, 0.3 ppb Sr, 0.02 ppb Sm, and 0.06 ppb Nd. Mass fractionation corrections for Sr and Nd isotope ratios were based on the values of $^{86}Sr/^{88}Sr = 0.1194$ and $^{146}Nd/^{144}Nd = 0.7219$. The measured values for the NBS-987 Sr standard and the JNdi-1 Nd standard are $^{87}Sr/^{86}Sr = 0.710239 \pm 10$ (2σ, $n = 6$), and $^{143}Nd/^{144}Nd = 0.512069 \pm 5$ (2σ, $n = 8$), respectively.

Re and Os isotopes were determined using a PE ELAN DRC-e ICP-MS in the National Research Center of Geoanalysis in Beijing, China. The concentrations of Re and Os were measured by isotope dilution. Sample preparation and analytical procedures are the same as those given in Du et al. (2004). The intensities of ^{190}Os and ^{185}Re were used to correct the interference between Os and Re. All measured ratios were corrected for oxygen isotopic interference, and mass fractionation and Os concentrations. The total procedural blanks contain ~ 0.003 ppb Re and 10–20 ppt Os. The internal standard JCBY (the Jinchuan sulfide ore) was used to monitor the accuracy of the measurements. The repeatedly measured Re and Os contents and $^{187}Os/^{188}Os$ ratio of this standard are 38.65 ± 0.12 ppb, 15.65 ± 0.05 ppb, and

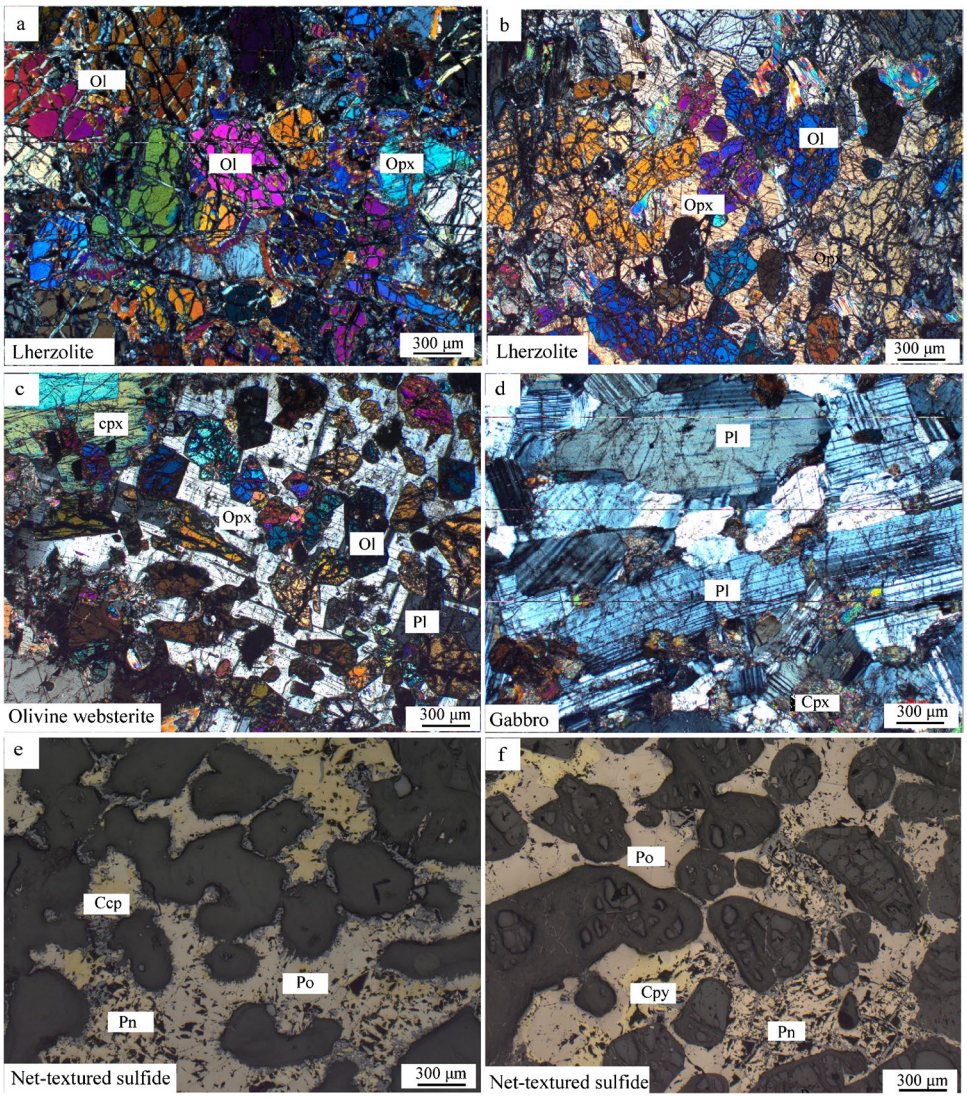

Fig. 4 Photomicrographs of the Tulaergen mafic–ultramafic rocks: lherzolite (**a**, **b**); olivine websterite (**c**); gabbro (**d**); net-textured sulfide (**e**, **f**). Ol = olivine, Opx = orthopyroxene, Cpx = clinopyroxene, Pl = plagioclase, Pn = pentlandite, Po = pyrrhotite, Cpy = chalcopyrite

0.3361 ± 0.0017, respectively, which are similar to the recommended values (38.61 ± 0.54 ppb, 16.23 ± 0.17 ppb, and 0.3363 ± 0.0029, Du et al., 2004).

Sulfur isotope analysis was carried out at Indiana University using the continuous flow method described in Studley et al. (2002). Coarse sulfide minerals such as pentlandite, chalcopyrite, pyrrhotite from Tulaergen ores samples and pyrites from the wall rocks were drilled from polished sections using a 0.75-mm carbide bit. Between 0.1 and 0.2 mg of sulfide powder was placed in tin cups with approximately 1.5 to 2 mg vanadium pentoxide (V_2O_5). Samples were prepared in an elemental analyzer by flash combustion at 1800 °C with a reactor column temperature of 1010 °C. Measurements of produced SO_2 were made using a Finnigan Delta V Stable isotope ratio mass spectrometer, with results reported in per mil delta notation relative to Vienna-Canyon Diablo Troilite (V-CDT). Analytical uncertainty was less than ± 0.05‰, and sample reproducibility was within ± 0.2‰. Sulfide standards used were IAEA-S1, IAEA-S2, IAEA-S3, with values of − 0.3, 21.7, and − 31.3‰, respectively, on the SO_2 scale.

The concentrations of Ni-Cu and S in the rock powder samples were measured by ICP-AES using a PE8300 machine and by combustion-iodometric titration using a LECO CS230 instrument in the National Research Center of Geoanalysis in Beijing, China. The concentrations of PGEs in the samples were determined by a combination of NiS fire assay PGE pre-concentration, Te co-precipitation, and ICP-MS analysis using a PE300D machine in the National Research Center of Geoanalysis in Beijing, China. The analytical errors are within ± 10%, as estimated from duplicate measurements of the international standards (UMT-1 and WPR-1) that were analyzed together with our samples.

Analytical results

Zircon U–Pb isotope age and Hf isotopes

The CL images of the dated zircon grains of a large lherzolite sample from the Tulaergen sulfide-mineralized ultramafic dyke are shown in Fig. 5a. The zircon grains are prismatic and mostly subhedral, with lengths from 40 to 100 µm, widths from 30 to 80 µm, and length to width ratios from 1.2 to 2. They are semi-transparent, showing broad zoning or homogeneity in the CL images (Fig. 5a). Their morphology, zoning patterns, and degrees of transparency are generally different from zircons in granitoids, but are typical for those in mafic–ultramafic rocks (Corfu et al. 2003).

The U–Pb data of the dated zircons from the Tulaergen ultramafic dyke are listed in Table 1. The Th and U concentrations of 21 grains are 336–12,259 ppm and 670–11,101 ppm, respectively, with Th/U ratios from 0.4 to 2.6. The weighted mean $^{206}Pb/^{238}U$ age is 281 ± 2 Ma (Fig. 5b), which is ~ 20 myr younger than the associated gabbroic intrusion (300.5 ± 3.2 Ma, San et al. 2010). The large age gap necessitates our reclassification of this mafic–ultramafic intrusive body from a single intrusion to an intrusive complex. The Lu–Hf data of the dated zircon grains from the Tulaergen ultramafic dyke are listed in Table 2. The calculated εHf (t = 281 Ma) is from 14 to 17, with an average of 16, which is similar to the depleted mantle value (Fig. 5c).

Mineral compositions

The compositions of Cr-spinel, olivine, clinopyroxene, and plagioclase are given as supplementary data (Table S2). Cr-spinel is rare in the Tulaergen ultramafic dyke. Cr-spinels in the lherzolite of the ultramafic dyke contain 21.5–22.8 wt% Al_2O_3 and 35.1–35.3 wt% Cr_2O_3, with $Mg^{\#}$ [100 Mg/(Mg + Fe^{2+}), molar] from 43 to 45 and $Cr^{\#}$ [100Cr/(Cr + Al), molar] from 51 to 52. The An contents of plagioclase and En contents of clinopyroxene in the dyke are between 70 and 77 mol% and between 50 and 51 mol%, respectively.

Olivine crystals in the Tulaergen ultramafic dyke contain 77.1–85.4 mol% Fo, 707–1807 ppm Ni, and 226–1186 ppm Ca (Fig. 6a, b). The Fo and Ni contents of olivines in the samples containing disseminated and net-textured sulfides from the different parts of the Tulaergen deposit exhibit a weak negative correlation (Fig. 6b). The samples from the western segment and the lower part of the middle segment plot together in one cluster, the

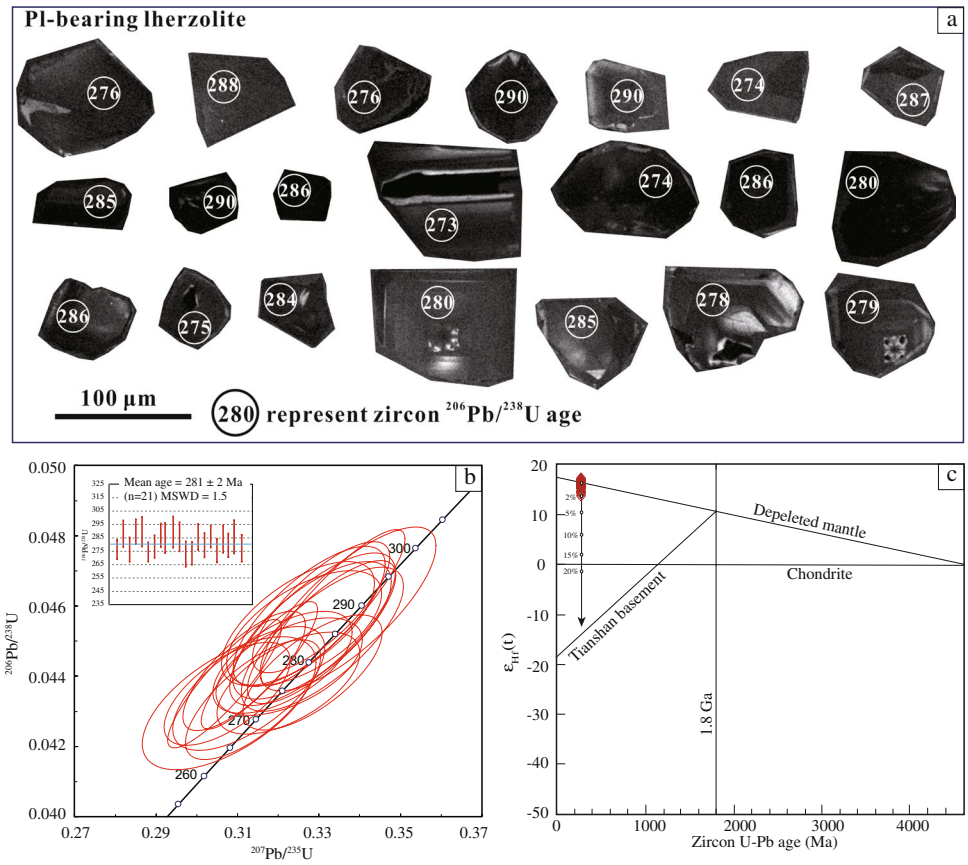

Fig. 5 **a** Cathodoluminescence images of zircon crystals from the Tulaergen ultramafic dyke. **b** Zircon Concordia diagram for the dyke. **c** Zircon $\varepsilon_{Hf}(t)$ versus U–Pb age for the dyke. The age of Tianshan basement is based on Hu et al. (2000), which was calculated using the parameters for the upper crust from Amelin et al. (1999)

Table 1 Concentrations of U, Th, and Pb, and U–Pb isotopes of zircons from the Tulaergen ultramafic dyke

Point number	Sample	Pb ppm	Th ppm	U ppm	Th/U	$^{207}Pb/^{206}Pb$	1σ	$^{207}Pb/^{235}U$	1σ	$^{206}Pb/^{238}U$	1σ	$t_{206/238}$ Ma	1σ
Pl-bearing lherzolite													
1	TLI-01	60	1235	875	1.41	0.05191	0.00110	0.31253	0.00716	0.04381	0.00059	276.4	3.7
2	TLI-02	127	2725	1758	1.55	0.05064	0.00099	0.31760	0.00763	0.04570	0.00082	288.1	5.0
3	TLI-03	700	12,259	11,101	1.10	0.04942	0.00077	0.29682	0.00572	0.04379	0.00075	276.3	4.6
4	TLI-04	295	6584	3892	1.69	0.05075	0.00082	0.32054	0.00688	0.04597	0.00076	289.7	4.7
5	TLI-05	150	3709	1728	2.15	0.05133	0.00090	0.32339	0.00725	0.04596	0.00090	289.6	5.6
6	TLI-06	89	2254	1182	1.91	0.04980	0.00094	0.29743	0.00632	0.04350	0.00060	274.5	3.7
7	TLI-08	44	336	791	0.42	0.05052	0.00117	0.31490	0.00767	0.04550	0.00072	286.9	4.4
8	TLI-11	152	2260	2346	0.96	0.04892	0.00108	0.30256	0.00719	0.04519	0.00092	284.9	5.7
9	TLI-12	132	1950	1916	1.02	0.05197	0.00123	0.32713	0.00882	0.04592	0.00095	289.4	5.9
10	TLI-13	186	4541	2220	2.05	0.05118	0.00120	0.31844	0.00829	0.04534	0.00089	285.8	5.5
11	TLI-14	48	1011	670	1.51	0.05037	0.00151	0.29799	0.00871	0.04324	0.00077	272.9	4.8
12	TLI-15	79	1286	1196	1.08	0.05105	0.00108	0.30383	0.00678	0.04333	0.00070	273.5	4.3
13	TLI-16	98	1143	1517	0.75	0.05115	0.00117	0.31829	0.00795	0.04531	0.00080	285.6	4.9
14	TLI-17	358	10,019	4170	2.40	0.05019	0.00087	0.30537	0.00583	0.04431	0.00074	279.5	4.6
15	TLI-18	72	1271	942	1.35	0.05068	0.00115	0.31641	0.00777	0.04537	0.00067	286.0	4.1
16	TLI-19	70	1452	986	1.47	0.05035	0.00109	0.30274	0.00761	0.04366	0.00072	275.5	4.4
17	TLI-20	184	2355	2827	0.83	0.05160	0.00096	0.32083	0.00814	0.04506	0.00084	284.1	5.2
18	TLI-21	70	885	1124	0.79	0.05078	0.00101	0.31109	0.00698	0.04439	0.00059	280.0	3.7
19	TLI-22	147	3026	1862	1.63	0.05142	0.00098	0.32072	0.00744	0.04525	0.00083	285.3	5.1
20	TLI-23	252	7051	2669	2.64	0.05230	0.00101	0.31839	0.00698	0.04411	0.00067	278.3	4.1
21	TLI-24	135	3808	1527	2.49	0.05105	0.00106	0.31265	0.00733	0.04428	0.00057	279.3	3.5

Table 2 Hf isotopes of zircon crystals from the Tulaergen ultramafic dyke

No	$^{176}Yb/^{177}Hf$	2σ	$^{176}Lu/^{177}Hf$	2σ	$^{176}Hf/^{177}H$	2σ	$(^{176}Hf/^{177}Hf)_i$	ε_{Hf}
TL I-1	0.055691	0.000601	0.001200	0.000010	0.283012	0.000021	0.283006	14.4
TL I-2	0.026236	0.001016	0.000560	0.000021	0.283039	0.000027	0.283037	15.5
TL I-3	0.138392	0.001851	0.003232	0.000092	0.283012	0.000030	0.282995	14.1
TL I-4	0.079292	0.000507	0.001690	0.000029	0.283091	0.000023	0.283082	17.2
TL I-5	0.061226	0.001478	0.001168	0.000020	0.283015	0.000018	0.283009	14.5
TL I-6	0.018655	0.000497	0.000435	0.000007	0.283073	0.000028	0.283071	16.7
TL I-8	0.097946	0.001977	0.002403	0.000090	0.283067	0.000029	0.283055	16.2
TL I-11	0.071445	0.001968	0.001701	0.000072	0.283053	0.000023	0.283044	15.8
TL I-12	0.017715	0.000292	0.000332	0.000003	0.283050	0.000019	0.283048	16.0
TL I-13	0.073767	0.000368	0.001495	0.000006	0.282990	0.000024	0.282982	13.6
TL I-14	0.026005	0.000830	0.000483	0.000013	0.283069	0.000019	0.283066	16.6
TL I-15	0.075972	0.000375	0.001521	0.000010	0.283039	0.000018	0.283031	15.3
TL I-16	0.136470	0.006056	0.002860	0.000103	0.283074	0.000031	0.283059	16.3
TL I-17	0.086647	0.001488	0.001939	0.000064	0.283059	0.000030	0.283049	16.0
TL I-18	0.130021	0.002549	0.002741	0.000064	0.283043	0.000030	0.283028	15.2
TL I-19	0.082702	0.003786	0.001808	0.000074	0.283081	0.000028	0.283072	16.8
TL I-20	0.073200	0.002483	0.001662	0.000046	0.283030	0.000023	0.283021	15.0
TL I-21	0.046270	0.000226	0.000821	0.000003	0.283049	0.000020	0.283045	15.8

ε_{Hf} calculated using the method of Blichert and Albarede (1997), ^{176}Lu decay constant $\lambda = 1.865 \times 10^{-11}$ year^{-1} (Soderlund et al. 2004), $t = 281$ Ma

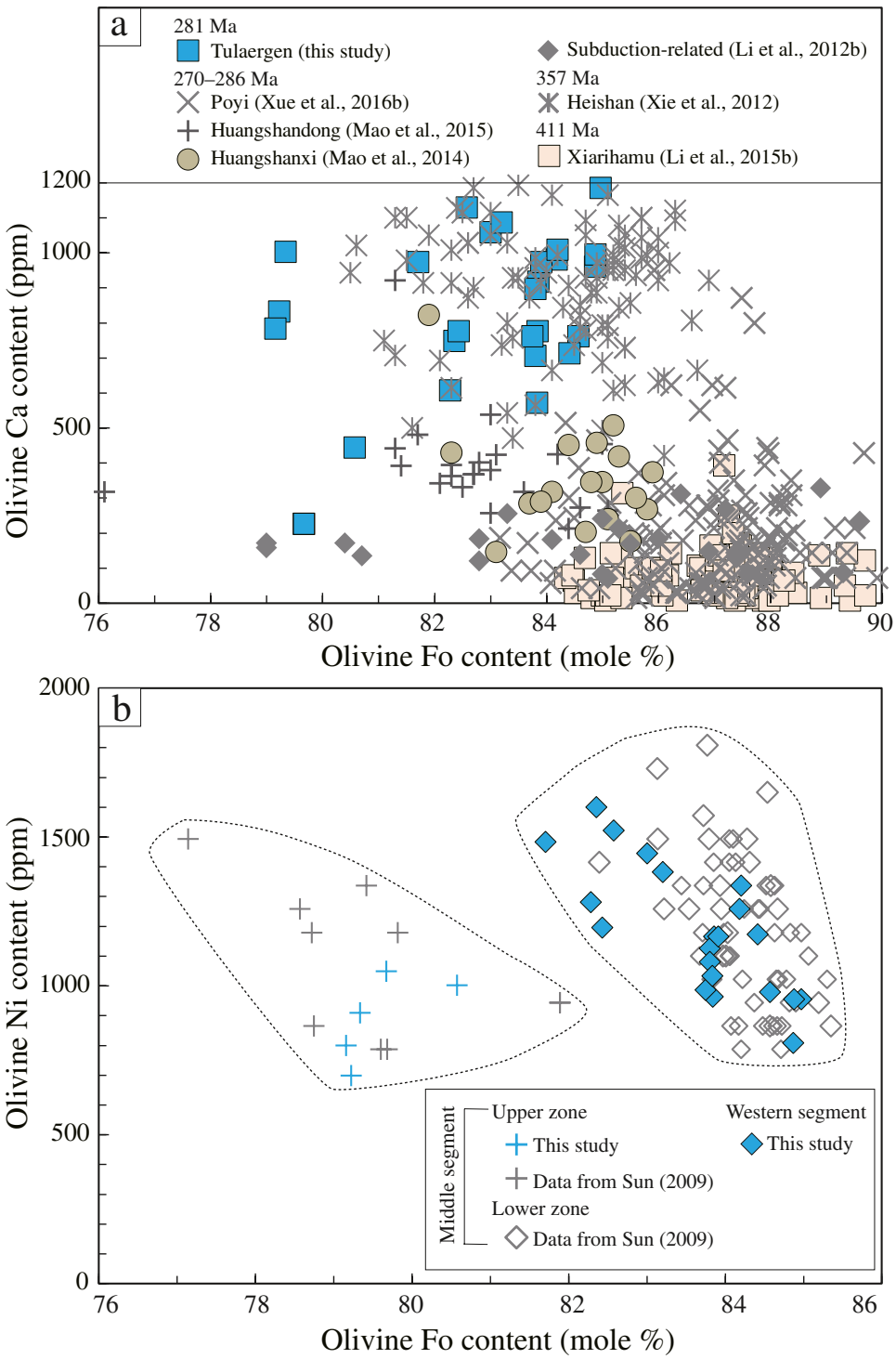

Fig. 6 Olivine Fo versus Ca (**a**) and Ni contents (**b**) for the Tulaergen sulfide-mineralized ultramafic dyke

samples from the upper zone of the middle segment plot in another cluster. The former have higher Fo contents (82–85 mol%) than the latter (77–82 mol%). The ranges of Ni contents in these two groups of olivine are similar, although the number of analyses for the upper part of the middle segment is very limited (Fig. 6b).

Whole-rock major and trace elements

The concentrations of major and trace elements in the samples from the Tulaergen mafic–ultramafic dyke and the standards used in this study are given as supplementary data (Table S3). A comparison of sulfide-poor whole-rock

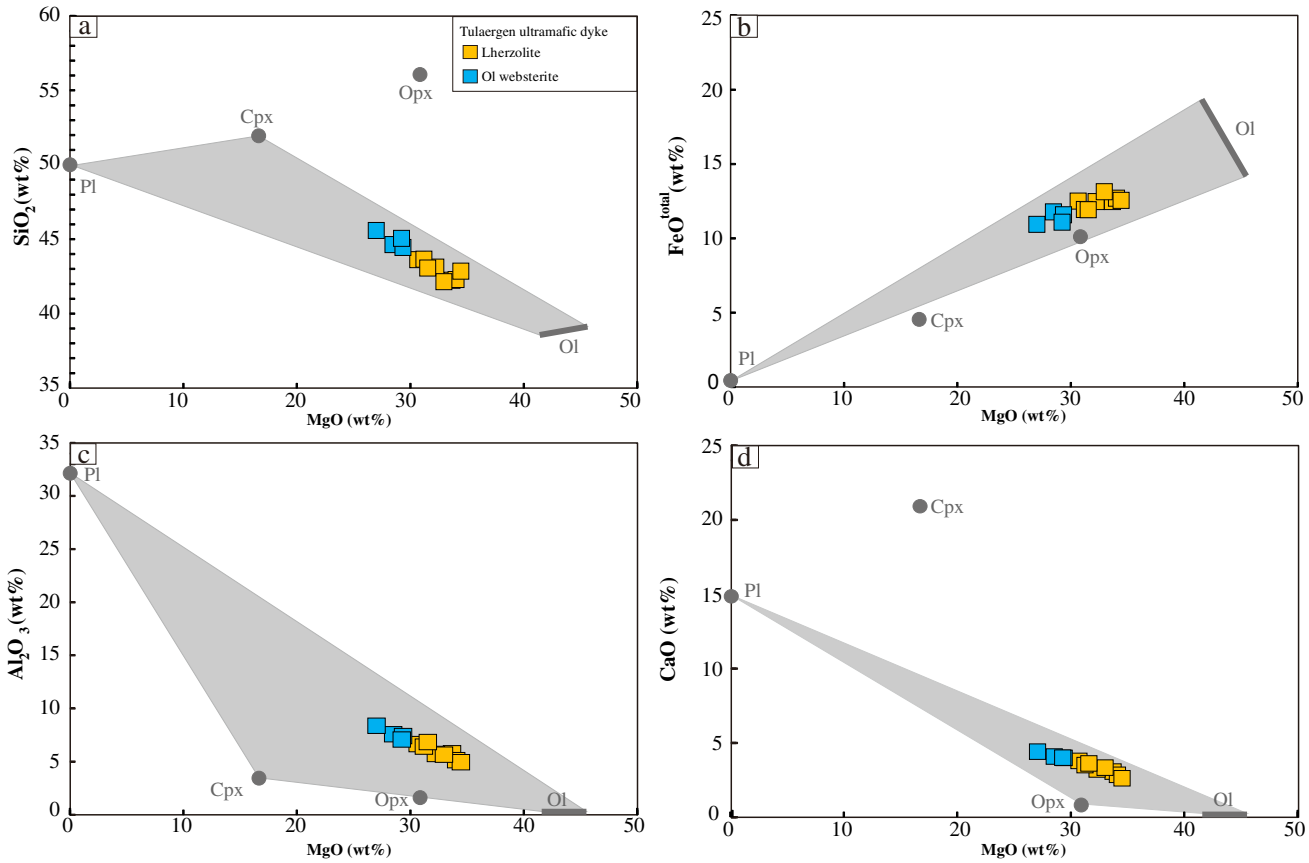

Fig. 7 Compositional comparison of whole rocks with major rock-forming minerals from the Tulaergen ultramafic rocks. Mineral abbreviations are the same as in Fig. 4

compositions with rock-forming mineral compositions is illustrated in Fig. 7. In the diagram, the whole-rock compositions are normalized to 100% on a loss on ignition-free basis. Lherzolites have higher MgO and lower FeO^T than olivine websterite, consistent with higher amounts of olivine in the former than the latter. The simple comparison reveals that the major element compositions of the Tulaergen ultramafic rocks are mainly controlled by the abundances of olivine, pyroxenes, and plagioclase.

The chondrite-normalized rare earth element (REE) and mantle-normalized immobile trace element patterns of sulfide-poor whole-rock samples from the Tulaergen ultramafic dyke are all shown in Fig. 8. The trace element patterns of the Tulaergen ultramafic rocks are remarkably similar to those of the Carboniferous (357 Ma; Xie et al. 2012) subduction-related Heishan sulfide-mineralized mafic–ultramafic intrusion in the nearby Beishan terrane (see Fig. 1b for location). The trace element patterns of the Tulaergen ultramafic rocks are also similar to those of the Early Permian basalts as well as the Carboniferous basalts in the region (see Fig. 1b for location). The abundances of the incompatible trace elements in the Tulaergen ultramafic rocks are 70–80% lower than in the basaltic lavas of East Tianshan as well as the Cenozoic arc basalts worldwide.

Chalcophile elements

The concentrations of S, Ni, Cu, and platinum-group elements (PGE) in the Tulaergen ultramafic rocks are listed in Table 3. For nickel, concentrations before and after correction for contribution from olivine are listed. The correction was made using the estimated olivine abundances and the average Ni content of olivine in the samples. The corrected Ni concentrations are used hereafter. The relationships between the chalcophile element abundances and S contents in the Tulaergen ultramafic rocks are illustrated in Fig. 9. At a given S content, samples from the upper zone of the middle segment tend to have lower Ni contents than those from the lower zone (Fig. 9a). Such difference is not present for Cu, mainly due to larger variation of Cu than Ni concentrations in the upper zone (Fig. 9b). Overall, a positive correlation with S contents is much stronger for Ni than for Cu (Fig. 9a, b). A positive correlation between PGEs and S contents also exists, but the degrees of such

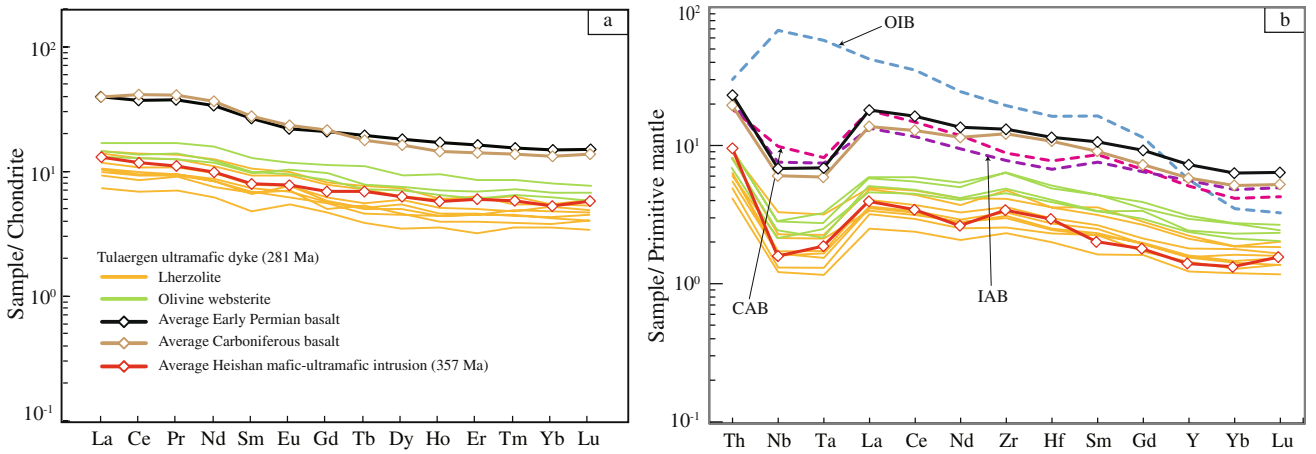

Fig. 8 Chondrite-normalized REE patterns and mantle-normalized immobile incompatible elements patterns for the Tulaergen ultramafic dyke. The normalization values are from Palme and O'Neill (2014). The average composition of the Carboniferous basalts in the East Tianshan–Beishan Orogenic Collage is from Bai et al. (2018). The average composition of the Early Permian basalts in the region is from Liu et al. (2016). The average composition of the subduction-related Heishan mafic–ultramafic intrusion in the region is from Xie et al. (2012). The average compositions of global OIB, CAB, and IAB are from Li et al. (2015a)

correlations are highly variable (Fig. 9c–h). The correlation between individual IPGE (Os, Ir, Ru, and Rh) and S contents is poor (Fig. 9c–f). The correlation between individual PPGE (Pt, Pd) and S contents is much stronger (Fig. 9g, h).

We have calculated the Ni, Cu, and PGE tenors (concentrations in 100% sulfides) in the samples containing > 0.5 wt% S from the Tulaergen deposit using the equation of Barnes and Lightfoot (2005). The mantle-normalized patterns of the metal tenors are illustrated in Fig. 10. All of the samples show significant PGE depletion relative to Ni and Cu, and fractionated PGE patterns due to relative IPGE depletion. The samples from the west segment and the lower zone of the middle segment have similar PGE patterns (Fig. 10a). Some of the disseminated sulfide samples from the upper zone of the middle segment have more fractionated PGE patterns than other disseminated sulfides, as well as all net-textured sulfide (Fig. 10b). For distinction, we call this type of disseminated sulfide mineralization a highly PGE-fractionated type. Most of the highly PGE-fractionated disseminated sulfides also show more severe decoupling between Pt and Pd than the other types of sulfide mineralization (Fig. 10b). Compared to the older, subduction-related Heishan magmatic sulfide deposit in the Beishan terrane (see Fig. 1b for location), the Tulaergen magmatic sulfide deposit is more depleted in all PGEs (Fig. 10a, b).

Sr-Nd-Os-S isotopes

The Sr–Nd isotope data of the Tulaergen sulfide-poor ultramafic rocks are listed in Table 4. The initial isotope ratios and ε_{Nd} (t) were calculated using the zircon U–Pb age of 281 Ma from this study (Fig. 5b). The $(^{87}Sr/^{86}Sr)_i$ and ε_{Nd} (t) ratios of the ultramafic rocks are from 0.7034 to 0.7036 and from 5.1 to 6.9, respectively. These values are similar to the Carboniferous–Permian basalts in the region, and are within the ranges of Cenozoic arc basalts worldwide (Fig. 11). The Tulaergen ultramafic rock samples also plot within the present-day mantle array of DePaolo and Wasserburg (1979).

Re-Os isotopes of the sulfide-mineralized ultramafic rocks are listed in Table 5. The Re and Os contents range from 3.2 to 138 ppb and from 0.02 to 0.97, respectively. The initial $^{187}Os/^{188}Os$ ratios and γOs values were calculated using the zircon U–Pb age of 281 Ma. The γOs(t) values range from + 605 to + 954, which are significantly higher than the mantle value (close to zero, Shirey and Walker 1998). The γOs(t) values of the samples from the western and middle segments are from + 607 to + 674 and from + 605 to + 937, respectively.

Sulfur isotopes of base metal sulfides in the Tulaergen magmatic Ni-Cu sulfide deposit and pyrites in the country rocks are listed in Table 6. The $\delta^{34}S$ values of the ore deposits and the country rocks range from − 0.3 to 1.47 ‰ and from − 2.81 to 2.33 ‰, respectively. The $\delta^{34}S$ values of ore deposits are within the range of the MORB mantle values (0 ± 2 ‰, Labidi et al. 2013) and the country rocks, but are lower than those of the Carboniferous subduction-related Heishan magmatic sulfide deposit in the nearby Beishan region (Xie et al. 2014). Our data show no correction between $\delta^{34}S$ and γOs(t) values for the Tulaergen deposit.

Table 3 Concentrations of S, Ni, and Cu (in wt%) and PGE (in ppb) in ultramafic rock samples from the Tulaergen magmatic Ni-Cu deposit

Sample no	Location	Depth (m)	Segment/zone	Host rock	Sulfide texture	S	Ni	Ni*	Cu	Os	Ir	Ru	Rh	Pt	Pd
TL-3	ZK1106	135	Middle/Upper	Ol websterite	Disseminated	0.53	0.11	0.08	0.03	0.07	0.05	0.07	0.08	1.41	4.16
TL-5	ZK1106	125	Middle/Upper	Ol websterite	Disseminated	2.01	0.34	0.31	0.17	0.26	0.22	0.32	0.22	7.83	12.1
TL-6	ZK1106	121	Middle/Upper	Ol websterite	Disseminated	2.38	0.36	0.33	0.22	0.18	0.2	0.26	0.32	7.63	12.5
TL-7	ZK1106	113	Middle/Upper	Ol websterite	Disseminated	1.71	0.27	0.24	0.14	0.15	0.11	0.14	0.19	7.69	7.69
TL-10	ZK1106	88	Middle/Upper	Lherzolite	Disseminated	1.04	0.15	0.09	0.06	0.08	0.07	0.09	0.11	2.68	3.94
TL-47	15–17 line	200	Middle/Upper	Lherzolite	Disseminated	3.66	0.68	0.62	0.49	0.09	0.1	0.11	0.17	43.8	18.9
TL-48	15–17 line	200	Middle/Upper	Lherzolite	Disseminated	4.87	0.79	0.73	0.71	0.14	0.09	0.08	0.13	47.8	14.5
TL-49	15–17 line	200	Middle/Upper	Lherzolite	Disseminated	3.67	0.64	0.58	0.38	0.12	0.08	0.1	0.37	45.6	14.1
15TL-01	15–17 line	200	Middle/Upper	Lherzolite	Disseminated	9.89	0.77	0.71	0.64	0.11	0.13	0.18	0.16	16	7.72
15TL-02	15–17 line	200	Middle/Upper	Lherzolite	Massive	36.5	2.79	2.73	4.00	0.93	1.07	1.09	8.14	79.9	72.4
15TL-03	15–17 line	200	Middle/Upper	Lherzolite	Disseminated	9.98	0.62	0.56	0.31	0.31	0.33	0.26	0.82	118	4.95
15TL-04	15–17 line	200	Middle/Upper	Lherzolite	Net-textured	12.03	0.95	0.89	0.15	0.35	0.35	0.35	1.01	24.6	58.7
15TL-05	15–17 line	200	Middle/Upper	Lherzolite	Net-textured	10.27	0.73	0.67	0.57	0.18	0.19	0.16	0.65	29.9	36.9
15TL-06	15–17 line	200	Middle/Upper	Lherzolite	Disseminated	1.66	0.13	0.07	0.06	0.14	0.1	0.14	0.41	3.84	5.98
15TL-07	15–17 line	200	Middle/Upper	Lherzolite	Disseminated	1.54	0.11	0.05	0.55	0.25	0.26	0.35	0.36	14.5	24.6
15TL-08	15–17 line	200	Middle/Upper	Lherzolite	Net-textured	15.3	1.47	1.41	1.25	0.79	0.77	0.72	1.27	28.2	20.4
15TL-12	15–17 line	200	Middle/Upper	Lherzolite	Disseminated	2.64	0.24	0.18	0.19	0.24	0.17	0.22	0.21	6.19	10.2
15TL-14	15–17 line	200	Middle/Upper	Lherzolite	Net-textured	12.61	1.01	0.95	1.65	0.71	0.45	0.54	0.58	14.1	35
15TL-15	15–17 line	200	Middle/Upper	Lherzolite	Disseminated	1.51	0.16	0.1	0.13	0.33	0.17	0.27	0.18	4.41	6.77
15TL-16	15–17 line	200	Middle/Upper	Lherzolite	Disseminated	6.45	0.57	0.51	1.39	0.13	0.11	0.09	0.24	46.5	68.6
15TL-19	15–17 line	200	Middle/Upper	Lherzolite	Disseminated	5.82	0.48	0.42	0.57	0.14	0.09	0.11	0.18	49.8	71.6
TL-36	Zk1501	500	Middle/Lower	Lherzolite	Disseminated	0.72	0.16	0.1	0.07	0.27	0.19	0.29	0.29	3.15	4.27
TL-38	Zk1501	467	Middle/Lower	Lherzolite	Sulfide-poor	0.46	0.11	0.05	0.01	0.41	0.14	0.17	0.09	1.9	2.24
TL-40	Zk1501	582	Middle/Lower	Lherzolite	Sulfide-poor	0.42	0.10	0.04	0.02	0.07	0.06	0.08	0.16	5.52	3.23
TL-41	Zk1501	572	Middle/Lower	Lherzolite	Disseminated	0.5	0.12	0.06	0.03	0.11	0.08	0.12	0.1	3.38	4.46
TL-43	Zk1501	542	Middle/Lower	Lherzolite	Disseminated	0.92	0.20	0.14	0.06	0.07	0.04	0.06	0.06	2.04	2.14
TL-45	Zk1501	520	Middle/Lower	Lherzolite	Disseminated	2.37	0.40	0.34	0.20	0.15	0.13	0.13	0.2	7.12	10.6
TL-46	Zk1501	516	Middle/Lower	Lherzolite	Disseminated	1.71	0.32	0.26	0.15	0.11	0.08	0.08	0.1	4.42	5.26
TL-12	ZK3302	558	Western	Ol websterite	Disseminated	0.6	0.14	0.11	0.04	0.13	0.08	0.15	0.09	1.94	2.84
TL-14	ZK3302	547	Western	Ol websterite	Sulfide-poor	0.49	0.14	0.11	0.03	0.07	0.06	0.09	0.08	2.23	2.88
TL-16	ZK3302	535	Western	Ol websterite	Disseminated	1.09	0.24	0.21	0.08	0.09	0.1	0.13	0.13	3.62	6.23
TL-18	ZK3302	524	Western	Ol websterite	Disseminated	1.53	0.28	0.25	0.13	0.14	0.12	0.18	0.17	4.19	7.13
TL-20	ZK3302	506	Western	Ol websterite	Sulfide-poor	0.42	0.12	0.09	0.03	0.54	0.37	0.85	0.13	1.82	2.35
TL-24	ZK3302	474	Western	Ol websterite	Sulfide-poor	0.42	0.12	0.09	0.02	0.18	0.05	0.07	0.08	2.06	2.41
TL-25	ZK3302	450	Western	Ol websterite	Sulfide-poor	0.38	0.13	0.1	0.02	0.29	0.06	0.09	0.09	1.38	1.67
TL-28	ZK3302	420	Western	Ol websterite	Sulfide-poor	0.097	0.09	0.06	0.01	0.06	0.03	0.06	0.05	0.88	1.23
TL-30	ZK3302	400	Western	Ol websterite	Sulfide-poor	0.17	0.09	0.06	0.01	0.06	0.11	0.1	0.08	1.09	1.53

Discussion

Tectonic significance of the Tulaergen mafic–ultramafic complex

As shown in Fig. 1b, the Tulaergen mafic–ultramafic complex is located in the North Tianshan-Heiyingshan arc terrane according to Xiao et al. (2010, 2015, 2019). These authors suggested that subduction in the region lasted until the end of the Early Permian. Based on the presence of ultramafic rocks in the center surrounded by gabbroic rocks in some of the Early Permian mafic–ultramafic intrusions in East Tianshan (Fig. 1b), Xiao et al. (2004) classified these intrusions as Alaskan-type complexes. However, none of the Early Permian mafic–ultramafic intrusions in the region used in the study of Xiao et al. (2004) shows the key feature of a typical Alaskan-type complex, i.e., concentric zonation within the ultramafic member (Taylor 1967).

The new results from this study show that the common features of an arc mafic–ultramafic complex such as the Duke Island complex in southern Alaska (Thakurta et al. 2008) are also present in the Tulaergen complex. For example, the age of the ultramafic member of this complex is ~ 20 myr younger than the surrounding gabbroic rocks (Fig. 3a, c). Based on this important feature, plus the regional geological constraints described above, we recognize the Tulaergen mafic–ultramafic complex to be an arc igneous complex. This new interpretation can be further tested using mineral chemistry and whole-rock trace elements and Sr–Nd-Hf isotopes. As shown in Fig. 6a, olivine crystals in the Tulaergen ultramafic rocks have low Ca contents (< 1200 ppm), which is common in arc basalts and mafic–ultramafic rocks, but extremely rare in continental flood basalts and associated mafic–ultramafic intrusions (see summary in Li et al. 2012b). As shown in Fig. 5c and Fig. 11, the isotope tracers indicate that crustal contamination in the Tulaergen magma is negligible. Hence, the pronounced negative Nb–Ta anomalies in the Tulaergen ultramafic rocks can be regarded as primary features, similar to many arc basalts (Fig. 8b).

The classification of the Tulaergen mafic–ultramafic complex as an arc igneous complex implies that other contemporaneous mafic–ultramafic intrusions in the region are also subduction-related. Previously, other researchers suggested that all of the Permian mafic–ultramafic intrusions in the region are linked to the Tarim mantle plume (e.g., Pirajno et al. 2008; Qin et al. 2011; Su et al., 2014; Zhang and Zou 2013), or lithospheric delamination coupled by asthenosphere upwelling in a post-subduction environment (e.g., Song et al. 2013, 2021; Han and Zhao 2018; Li et al. 2019). These two competing models are all based on the same assumption that the Tarim Craton and the micro-continents and associated arc terranes to the north were amalgamated by the end of the Carboniferous, which in turn is based on the geology of Western Tianshan, not that of the East Tianshan–Beishan region where these intrusions are located (see Fig. 1a and b for locations). As described above, the geology of this region clearly support the view that subduction in the region lasted until the end of the Early Permian (Xiao et al. 2010, 2015, 2019). Moreover, an age gap of ~ 20 myr between the mafic and ultramafic members of the Tulaergen complex (Fig. 3a, c) is clearly inconsistent with the plume model. Mantle plume activity may last for a protracted time, but the plate overlying the plume keeps moving (Morgan 1971), producing a hot-spot track such as the Hawaiian volcano train in which the distance between two volcanos with an age difference of 20 myr is ~ 2000 km (Wessel and Kroenke 2009). Interplay between a mantle plume and continental rifting could extend the duration of mafic magmatism at the same location, such as the East African Rift System (c.f., Koptev et al. 2018) and the Mid-continent Rift System in North America (c.f., Fairchild et al. 2017). However, compelling evidence for continental rifting in the East Tianshan–Beishan region has not been found.

PGE tenor modeling and its implication

The highly PGE-fractionated disseminated sulfides from the upper zone of the middle segment (Fig. 10b) are consistent with the compositions of significantly fractionated sulfide liquids due to MSS fractional crystallization, as IPGE (Os. Ir, Ru) plus Rh are compatible whereas PPGE (Pt, Pd) are incompatible in the MSS structure (e.g., Li et al. 1996). Significant decoupling between Pd and Pt in most of these samples (Fig. 10b) may have resulted from Pt-mineral fractionation during sulfide liquid solidification on cooling and post-magmatic redistribution of Pd due to hydrothermal alteration, which has been used to explain this kind of phenomena in other magmatic sulfide deposits (e.g., Dare et al. 2010; Prichard et al. 2013).

As shown in Fig. 9, among all IPGEs and Rh has the best correlation with S. Hence, we use Rh to represent this grouping. Rh, together with Pd and Pt are then used to evaluate the relative effects of *R*-factor and MSS fractional crystallization on the tenor variations in the Tulaergen deposit. Due to extremely high *D* values for PGE (e.g., Mungall and Brenan 2014), the concentrations of these metals in a sulfide liquid depend on both *R*-factor and their initial contents in magma (Campbell and Naldrett 1979). Hence, it is essential to set a minimum *R*-factor using other chalcophile elements with lower *D* values such as Ni or Cu. Due to the effects of olivine fractional crystallization and Fe–Ni exchange between olivine and sulfide liquid, it is difficult to know the initial content of Ni in the magma. Thus, we chose Cu for the estimation. The content of Cu in the most primitive Permian basalts in East Tianshan is ~ 100 ppm (Liu et al. 2016),

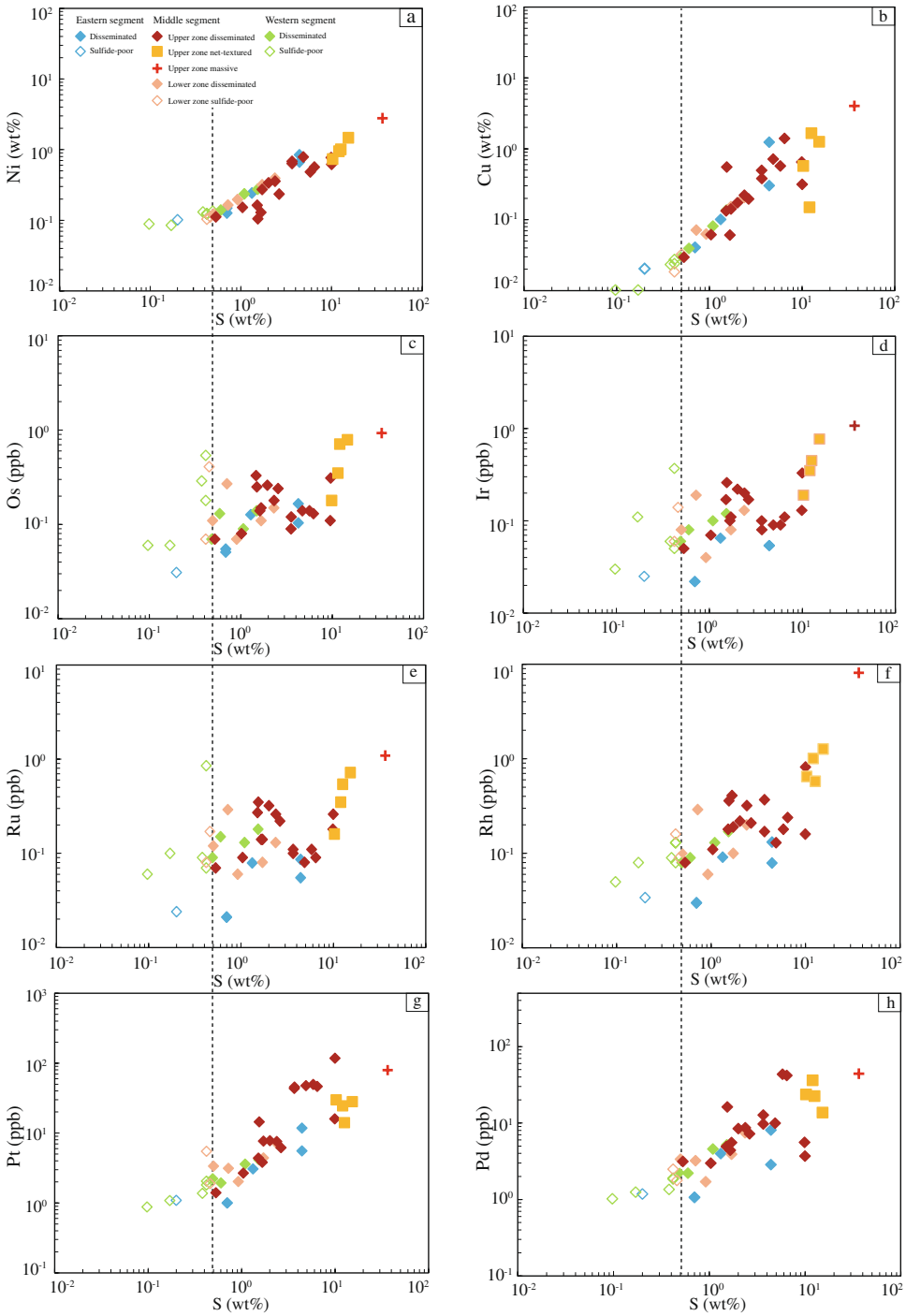

Fig. 9 Plots of chalcophile element concentrations versus S content in whole rocks from the Tulaergen magmatic Ni-Cu sulfide deposit

which is similar to the upper limit of arc basalts worldwide (Lee et al. 2012). Using this value to represent the initial content of Cu in the Tulaergen deposit, an experimental D_{Cu} of 1000 for a basaltic system (Ripley et al. 2002; Mungall and Brenan 2014), and the lowest Cu tenor of the disseminated sulfides in the Tulaergen deposit, which is ~ 1.4 wt%, the minimum *R*-factor is estimated to be ~ 150. With this in mind, we then use the partition coefficients of ~ 10^5 for PGEs between sulfide melt and silicate magma in basaltic systems, which are within the range of experimental results (Mungall and Brenan 2014), to estimate the range of *R*-factors and initial concentrations of Rh, Pt, and Pd in the parental magma for the Tulaergen deposit. The estimated range of *R*-factors is from 150 to 700. The estimated initial element concentrations in the magma are 0.009 ppb Rh, 0.32 ppb Pt, and 0.52 ppb Pd, which are similar to the estimated values for some other Permian magmatic sulfide deposits in the region such as Huangshanxi and Huangshandong (Mao et al.

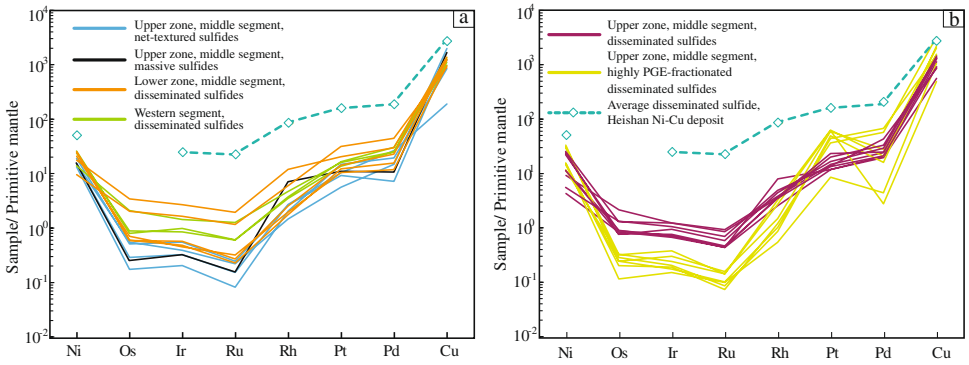

Fig. 10 Mantle-normalized Ni-PGE-Cu patterns for the Tulaergen magmatic Ni-Cu deposit. The primitive mantle values are from Palme and O'Neill (2014)

2014, 2015). The estimated initial PGE concentrations in the Tulaergen magma are approximately one order of magnitude lower than those of the Grenada arc picritic basalts (Woodland et al. 2002). The Grenada arc picritic arc basalts have the highest PGE contents among all global arc basalts that have been analyzed for PGE contents to date. Such a difference supports the notion that the parental magma for the Tulaergen deposit experienced previous interaction with sulfide liquids, either in the staging chamber or the mantle source, or both.

Magma differentiation and sulfide saturation

Magmatic Ni-Cu sulfide deposits are mainly hosted in mafic–ultramafic intrusions formed from magma produced by mantle partial melting (Naldrett 2011). The first olivine that crystallizes from the primary mantle-derived magma usually has similar Fo content to that of olivine in the mantle residue, i.e., between 89 and 93 mol% (e.g., Schmidberger and Francis 1999). By definition, primary mantle-derived magma is the original mantle partial melt without any fractional crystallization and crustal contamination. The Fo contents of olivine in the Tulaergen complex are from 77.1 to 85.4 mol%, significantly lower than that of olivine crystallizing from a primary mantle-derived melt. The simple comparison indicates that the parental magma for the Tulaergen deposit is a differentiated liquid. Low Ni/Cu ratios of the bulk sulfide ores provide another support for this interpretation. The average Ni/Cu ratio of bulk sulfide ores in the Tulaergen deposit is ~ 2, which is 4 times lower than that of the Xiarihamu subduction-related magmatic sulfide deposit (~ 8) hosted by ultramafic rocks with olivine Fo contents as high as 90 mol% (Li et al. 2015b).

Zircon Hf isotopes and whole-rock Sr–Nd indicate that the parental magma of the Tulaergen deposit was not contaminated with the Pre-Carboniferous meta-sedimentary rocks of the Tianshan basement, which could also be present at depth in the Tulaergen area, or that the amount of such contamination is negligible. As shown in Fig. 5c, the εHf (t) values of zircons from the host rock are from 13 to 18, with an average value similar to that of the depleted mantle, supporting the argument against contamination with the crust. The Tulaergen mafic–ultramafic intrusive rocks, and the Permian basalts (data from Liu et al. 2016) and Carboniferous arc basalts (data from Xie et al. 2016; Zhang et al. 2017) in the region have similar Sr–Nd isotope compositions. The similarities prevent using Sr–Nd isotopes to estimate the amount of contamination by the volcanic rocks. Contamination of the Tulaergen magma by the Paleozoic sedimentary rocks in the region cannot be evaluated using Sr–Nd isotopes either, because currently there are no Sr–Nd isotope data for such potential contaminants. Insignificant amount of contamination with Pre-Carboniferous meta-sedimentary rocks, which may occur at depth, is indicated by the Sr–Nd isotope data (Fig. 11). The presence of Pre-Carboniferous meta-sedimentary rocks at depth in East Tianshan is indicated by the presence of abundant detrital zircons of Pre-Carboniferous ages in the Permian sandstones of this region (Zhang et al. 2016).

Sulfur isotopes indicate that selective assimilation of sulfides from the Carboniferous volcanic-sedimentary country rocks and the xenoliths of such rocks is possible. As shown in Fig. 12, the $\delta^{34}S$ values of sulfide minerals in the Tulaergen deposit are from − 0.3 to 1.47‰, which are within the range of the MORB mantle values (0 ± 2‰; Labidi et al. 2013) as well as the range of pyrites in the volcanic-sedimentary country rocks of the Tulaergen deposit. The presence of reacted xenoliths of the country rocks in the deposit (Wang et al. 2018) indicates that the addition of sulfur from the breakdown of pyrite in the xenoliths to the magma must have occurred, but the exact amount cannot be determined using S isotope data because the end-members have similar sulfur isotope compositions.

The γOs values (605–954) of the Tulaergen deposit are significantly higher than typical mantle values (close to zero; Shirey and Walker 1998) and are consistent with

Table 4 Sr–Nd isotopes of the Tulaergen ultramafic rocks

Sample no	Rock type	Rb (ppm)	Sr (ppm)	$^{87}Rb/^{86}Sr$	$^{87}Sr/^{86}Sr$	2σ	Sm (ppm)	Nd (ppm)	$^{147}Sm/^{144}Nd$	$^{143}Nd/^{144}Nd$	2σ	$(^{87}Sr/^{86}Sr)_i$	$\varepsilon_{Nd(t)}$
TL-3	Ol websterite	9.83	172	0.165081	0.704225	0.000007	1.47	5.60	0.158148	0.512909	0.000010	0.703555	6.70
TL-12	Lherzolite	5.36	119	0.130164	0.704054	0.000007	0.71	2.77	0.154151	0.512818	0.000010	0.703526	5.06
TL-24	Lherzolite	5.53	93.1	0.171724	0.704170	0.000007	1.08	3.90	0.168193	0.512872	0.000008	0.703474	5.60
TL-28	Ol websterite	9.58	138	0.201425	0.704199	0.000005	1.91	7.22	0.159844	0.512925	0.000008	0.703382	6.94
TL-30	Ol websterite	17.8	99.8	0.516001	0.705470	0.000008	1.92	6.70	0.173284	0.512942	0.000006	0.703378	6.80
TL-36	Lherzolite	7.82	126	0.179911	0.704136	0.000005	1.15	4.39	0.158780	0.512912	0.000010	0.703407	6.73
TL-40	Lherzolite	7.98	147	0.157479	0.704185	0.000005	1.55	5.58	0.168186	0.512845	0.000012	0.703547	5.08

ε_{Nd} is the derivation in parts per 10,000 of the initial ratio from that of a chondritic reservoir at the crystallization age of 281 Ma for ultramafic rocks

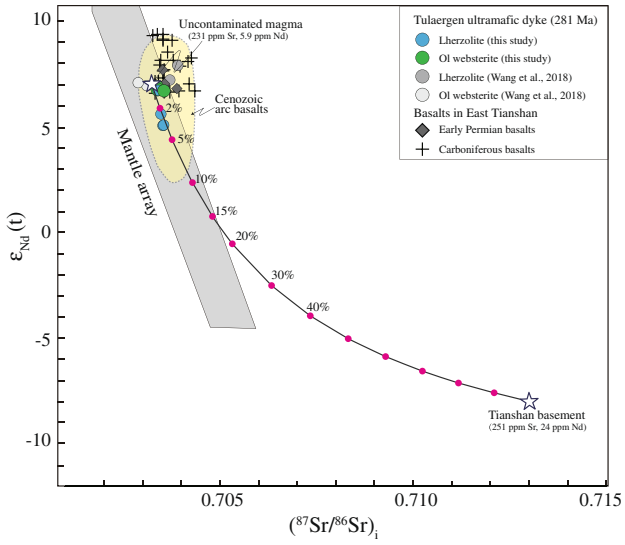

Fig. 11 Plot of whole-rock $(^{87}Sr\text{-}^{86}Sr)_i$ versus $\varepsilon_{Nd}(t)$ for the Tulaergen ultramafic rocks. The mantle array is from DePaolo and Wasserburg (1979). Values used in the mixing calculations are as follow: mantle-derived magma, 5.9 ppm Nd, 231 ppm Sr, $\varepsilon_{Nd}=7.00$ and $(^{87}Sr\text{-}^{86}Sr)_i=0.7032$; Tianshan basement, 24 ppm Nd, 251 ppm Sr, $\varepsilon_{Nd}(total)=-8$ and $(^{87}Sr\text{-}^{86}Sr)_i=0.713$. Sources of Sr–Nd isotopes for different types of rocks in the East Tianshan–Beishan Orogenic Collage: data for the Early Permian basalts are from Liu et al. (2016); data for the Carboniferous basalts are from Xie et al. (2016) and Zhang et al. (2017); data for the Tianshan basement are from Chen et al. (2000); data for mantle-derived magma are from Schmidt and Jagoutz (2017); The Sr–Nd isotopes of global Cenozoic arc basalts are from a public database (http://www.petdb.org)

selective assimilation of Os-bearing phases in the sedimentary country rocks, such as pyrite and/or organic matter. It is likely that fluid was involved in the transfer of S (and Os) from the potential contaminants in the contact aureole and xenoliths to the magma (Ripley and Li 2013). This, together with the lack of Os isotope data for the contaminants, prevents a more detailed evaluation. The possibility that organic matter could be involved during magma-rock interaction at Tulaergen is worth a detailed investigation, because the reduction of relatively oxidized magma, such as some arc basaltic melts, could lead to sulfide saturation (Thakurta et al. 2008; Tomkins et al. 2012).

In summary, our data show that fractional crystallization, the addition of external sulfur, and perhaps also organic matter from the country rocks in the contact aureole and entrained xenoliths, all of which have positive effects on sulfide saturation in basaltic magma (e.g., Ripley and Li 2013), were involved in the formation of the Tulaergen magmatic sulfide deposit. However, the relative contribution of these processes to the attainment of sulfide saturation in the Tulaergen magma is yet to be determined in the absence of additional data.

Table 5 Re-Os isotopic compositions of the Tulaergen magmatic Ni-Cu sulfide deposit

Sample no	Location	Depth (m)	Segment/zone	Host rock	Sulfide texture	Re (ppb)	Os (ppb)	$^{187}Re/^{188}Os$	1σ	$^{187}Os/^{188}Os$	1σ	$(^{187}Os/^{188}Os)_i$	γOs
TL05	ZK1106	125	Middle/Upper	Ol websterite	Disseminated	8.452	0.1528	268.2	2.8	2.159	0.009	0.8824	605
TL06	ZK1106	121	Middle/Upper	Ol websterite	Disseminated	9.795	0.1539	308.3	3.1	2.482	0.004	1.0147	711
15TL-02	15–17 line	200	Middle/Upper	Lherzolite	Massive	137.9	0.9687	700.0	7.1	4.431	0.007	1.0991	779
15TL-03	15–17 line	200	Middle/Upper	Lherzolite	Disseminated	30.39	0.3019	485.6	4.9	3.582	0.005	1.2707	916
15TL-05	15–17 line	200	Middle/Upper	Lherzolite	Disseminated	31.04	0.1322	1136	11	6.465	0.009	1.0571	745
15TL-07	15–17 line	200	Middle/Upper	Lherzolite	Net-textured	3.200	0.0213	726.3	7.3	4.776	0.008	1.3190	954
15TL-08	15–17 line	200	Middle/Upper	Lherzolite	Net-textured	74.78	0.6011	601.7	6.1	4.131	0.006	1.2676	913
15TL-09	15–17 line	200	Middle/Upper	Lherzolite	Net-textured	9.281	0.0660	679.8	6.9	4.379	0.007	1.1431	814
TL45	ZK1501	520	Middle/Lower	Lherzolite	Disseminated	10.56	0.1233	414.1	4.2	3.243	0.005	1.2724	917
TL46	ZK1501	516	Middle/Lower	Lherzolite	Disseminated	8.115	0.0849	461.5	4.7	3.494	0.005	1.2977	937
TL16	ZK3302	535	Western	Ol websterite	Disseminated	4.903	0.0911	258.0	2.6	2.113	0.004	0.8845	607
TL18	ZK3302	524	Western	Ol websterite	Disseminated	6.204	0.0999	300.6	3.0	2.399	0.004	0.9685	674

$\lambda = 1.666 \times 10^{-11}$/year, T = 281 Ma; the primitive initial $^{187}Os/^{188}Os$, $(^{187}Os/^{188}Os)_i$, is assumed to be 0.09531 and the average $^{187}Re/^{188}Os$ of chondrites is 0.40186 (after Shirey and Walker 1998)

Conduit-style mineralization at Tulaergen

Since the extensive geologic evaluation of the Voisey's Bay deposit of Labrador between 1996 and 2000, it has become clear that magma conduits are important sites of Ni-Cu-(PGE) sulfide mineralization (Lightfoot and Naldrett 1999; Li and Naldrett 1999, 2000). Previous to this time, models for the generation of the sulfide-rich ores at Noril'sk included formation within an open-system magma conduit (e.g., Naldrett et al., 1992; Arndt et al. 2003), but questions remained regarding specific application of a conduit model to Noril'sk versus a more encompassing application to magmatic Ni-Cu-PGE deposits in general. Given that most subhorizontal, mafic magmatic bodies in the upper crust (e.g., shallow magma chambers, sills, lava flows) are sourced from the mantle, magma conduits should be associated with all such occurrences. The only notable exception is the Sudbury Igneous Complex, whose melt sheet was largely created by upper crustal melting following a large meteor impact (e.g., Keays and Lightfoot 2004).

The "plumbing" system through which mafic magma ascends from its mantle source to intermediate or final accumulation in the upper crust may have horizontal and vertical components (e.g., Marsh 2006). Because of tectonism and erosion, it is rare that a conduit linked to a particular intrusion or lava flow can be definitely identified. However, detailed drilling to outline orebodies clearly identifies a dyke connecting a lower intrusion to an upper intrusion at Voisey's Bay. This provides compelling evidence to support the interpretation that the sulfide-mineralized dyke of the Voisey's Bay deposit is a magma conduit (Lightfoot and Naldrett 1999; Li and Naldrett 1999, 2000). Within the feeder dyke of the Voisey's Bay deposit, the most significant sulfide mineralization occurs at four principal localities: (1) the center of a steeply dipping segment of the dyke, (2) the widened part of the dyke, (3) the elbow of the dyke, and (4) the base of a gentle dip in the dyke. In addition, abundant massive sulfide ores also occur at the exit of the feeder dyke to the upper chamber (the upper intrusion). Such distributions are generally consistent with fluid dynamics of a heterogeneous ascending/flowing magma body (Lightfoot and Naldrett 1999; Li and Naldrett 1999; Ripley and Li 2011; Barnes and Mungall 2018).

Based on similar geometry, internal lithological structure and sulfide distribution between the Tulaergen dyke-hosted deposit (Fig. 3b–d) and the feeder dyke of the Voisey's Bay deposit, the Tulaergen deposit can be classified as a conduit-type magmatic sulfide deposit. As shown in the cross-sections and a long section (Fig. 3c, d), there are two sulfide-rich zones, separated by a thin neck of sulfide-poor rocks in the sub-vertical part of the Tulaergen ultramafic dyke. The Fo contents of olivines are clearly lower in the upper zone than the lower zone (Fig. 6b). The PGE tenors of net-textured sulfide ore are also lower in the upper zone than the lower zone, corresponding to

Table 6 S isotopes of sulfide separates from the Tulaergen deposit and country rocks

Sample	Location	Depth (m)	Segment/Zone	Host rock	Sulfide texture	$\delta^{34}S$
Ore samples						
TL-05	ZK1106	125	Middle/Upper	Ol websterite	Disseminated	0.7
TL-06	ZK1106	121	Middle/Upper	Ol websterite	Disseminated	0.58
TL-07	ZK1106	113	Middle/Upper	Ol websterite	Disseminated	0.28
TL-10	ZK1106	88	Middle/Upper	Lherzolite	Disseminated	0.69
15TL-01	15–17 line	200	Middle/Upper	Lherzolite	Disseminated	0.46
15TL-02	15–17 line	200	Middle/Upper	Lherzolite	Massive	0.74
15TL-03	15–17 line	200	Middle/Upper	Lherzolite	Disseminated	0.6
15TL-03		*Duplicate analysis*				*0.02*
15TL-04	15–17 line	200	Middle/Upper	Lherzolite	Net-textured	0.14
15TL-05	15–17 line	200	Middle/Upper	Lherzolite	Net-textured	–0.22
15TL-06	15–17 line	200	Middle/Upper	Lherzolite	Disseminated	0.00
15TL-08	15–17 line	200	Middle/Upper	Lherzolite	Net-textured	–0.03
15TL-09	15–17 line	200	Middle/Upper	Lherzolite	Net-textured	0.47
15TL-12	15–17 line	200	Middle/Upper	Lherzolite	Disseminated	0.68
15TL-13	15–17 line	200	Middle/Upper	Lherzolite	Disseminated	0.53
15TL-14	15–17 line	200	Middle/Upper	Lherzolite	Net-textured	–0.10
15TL-14		*Duplicate analysis*				*–0.05*
15TL-15	15–17 line	200	Middle/Upper	Lherzolite	Disseminated	0.17
15TL-16	15–17 line	200	Middle/Upper	Lherzolite	Disseminated	-0.3
15TL-19	15–17 line	200	Middle/Upper	Lherzolite	Disseminated	0.47
TL-33	ZK1501	424	Middle/Lower	Lherzolite	Disseminated	–0.10
TL-36	ZK1501	500	Middle/Lower	Lherzolite	Disseminated	0.13
TL-41	ZK1501	572	Middle/Lower	Lherzolite	Disseminated	0.20
TL-43	ZK1501	542	Middle/Lower	Lherzolite	Disseminated	0.48
TL-45	ZK1501	520	Middle/Lower	Lherzolite	Disseminated	0.17
TL-45		*Duplicate analysis*				*0.25*
TL-46	ZK1501	516	Middle/Lower	Lherzolite	Disseminated	0.89
TL-12	ZK3302	558	Western	Ol websterite	Disseminated	–0.01
TL-12		*Duplicate analysis*				*0.27*
TL-16	ZK3302	535	Western	Ol websterite	Disseminated	0.93
TL-18	ZK3302	524	Western	Ol websterite	Disseminated	0.18
TL-20	ZK3302	506	Western	Ol websterite	Disseminated	1.47
TL-25	ZK3302	450	Western	Ol websterite	Disseminated	–0.15
Carboniferous volcanic-sedimentary rocks collected from mining tunnel of 200 m and 250 m						
Sample	$\delta^{34}S$	Sample	$\delta^{34}S$	Sample	$\delta^{34}S$	
20TL1-01	0.19	20TL3-01	2.30	20TL4-08	–1.01	
20TL1-02	0.14	20TL3-02	–2.81	20TL4-09	–0.42	
21TL1-03	0.31	20TL3-03	–2.30	20TL4-10	–0.77	
20TL1-04	–0.29	20TL4-01	–0.17	20TL4-11	–0.80	
20TL1-05	–0.08	20TL4-02	–0.11	20TL5-01	–1.92	
20TL1-06	–0.53	20TL4-03	–0.48	20TL5-02	–0.58	
20TL2-01	1.42	20TL4-04	–0.16	20TL5-03	–1.40	
20TL2-02	2.33	20TL4-05	0.77	20TL5-04	–1.27	
20TL2-03	1.68	20TL4-06	–0.42	20TL5-05	–0.36	
20TL2-04	1.14	20TL4-07	–0.87	20TL5-07	–0.33	

$\delta^{34}S$ values are in per mil (‰), relative to V-CDT

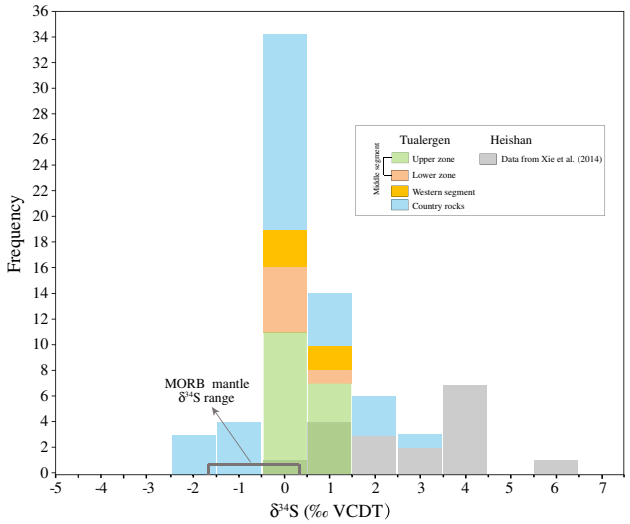

Fig. 12 Histogram of $\delta^{34}S$ values of sulfides from the Tulaergen Ni-Cu deposit and the subduction-related Heishan Ni-Cu deposit (data from Xie et al. 2014). The range of $\delta^{34}S$ for mid-ocean ridge basalts (MORB) is from Labidi et al. (2013)

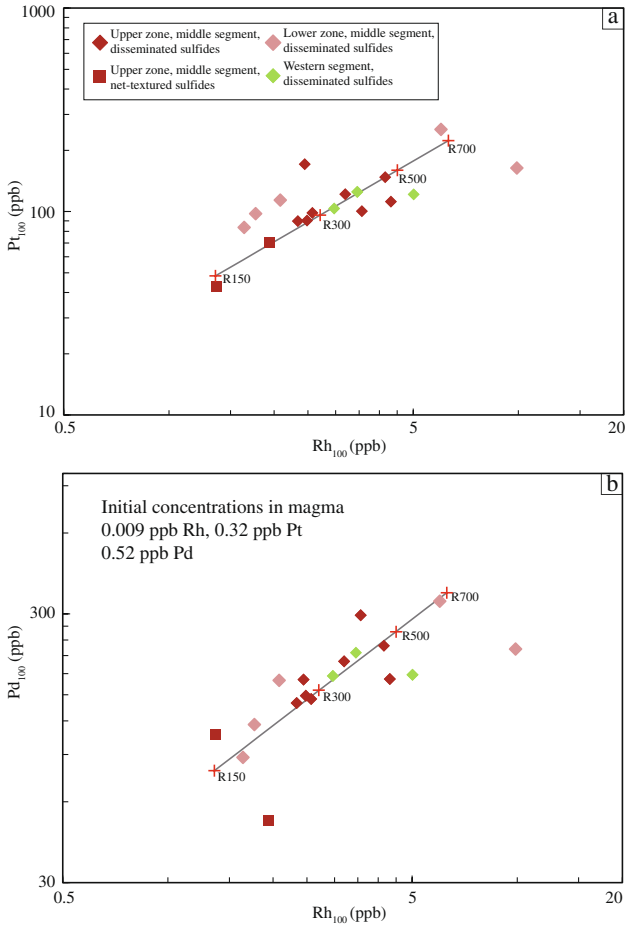

Fig. 13 Modeling of Pt, Pd and Rh tenor variations as a function of variable R-factors during sulfide segregation for the Tulaergen magmatic sulfide deposit. Modeling parameters: $D_{Rh} = 10^5$, $D_{Pt} = 10^5$, and $D_{Pd} = 10^5$

lower R-factors for the former according to our interpretation (Fig. 13). The physical separation and contrasting compositions between these two zones are consistent with two separate magma pulses charged with olivine crystals and immiscible sulfide droplets. The presence of multiple, subparallel sulfide-rich zones in the western, sub-horizontal part of the ultramafic dyke (Fig. 3c, d) suggests that there were at least two separate pulses of sulfide-bearing magma using the conduit system.

As described above, the Tulaergen ultramafic dyke is composed of olivine cumulates. Two common processes to form such rocks are gravitational accumulation in a large magma chamber or flow differentiation of olivine-charged magma in a dynamic conduit that supplies magma to a higher-level chamber or volcano. Obviously, the former interpretation is at odds with the size, geometry, and internal lithological structure of the host intrusive body of this deposit. Therefore, we conclude that the Tulaergen deposit formed from ascending magma charged with olivine crystals and immiscible sulfide droplets, similar to the model proposed previously for the Eagle and Tamarack conduit-type deposits (Ding et al. 2012; Taranovic et al. 2015).

Conclusions

Our new zircon U–Pb isotope age reveals for the first time that the Tulaergen ultramafic dyke was emplaced at 281 ± 2 Ma, ~ 20 myr younger than the surrounding gabbroic rocks. Such a large age gap is characteristic of some arc mafic–ultramafic complexes elsewhere in the world. Zircon Hf isotopes and whole-rock Sr–Nd isotopes indicate that the parental magma for the Tulaergen ultramafic dyke experienced insignificant bulk contamination with the crust. Hence, the observed pronounced negative Nb–Ta anomalies, coupled with light REE enrichments in the ultramafic rocks can be regarded as original features of the mantle-derived magma. Such geochemical features are characteristic of arc basalts worldwide. These new findings allow us to conclude that the Tulaergen mafic–ultramafic complex is linked to Early Permian arc basaltic magmatism. The geometry of the Tulaergen ultramafic dyke, sulfide distribution and metal tenor variations, and olivine Fo-Ni systematics support our new interpretation that the Tulaergen deposit is a conduit-type deposit formed from at least two pulses of ascending magma charged with olivine crystals and immiscible sulfide droplets. Elevated γOs values (+ 605 to + 954) of the sulfide ores support the notion that the addition of Os-bearing organic matter from sedimentary country rocks played a role in triggering sulfide saturation. The $\delta^{34}S$ values are from − 0.3 to 1.47‰, which are within the range of mantle values as well as that of the country rocks, providing inconclusive evidence for the role of external sulfur in

ore genesis. Fractional crystallization at depth for the parental magma of the Tulaergen deposit is indicated by significantly low olivine Fo contents, but the contribution of such a process to sulfide saturation in the magma requires further investigation. Modeling results indicate that the parental magma for the Tulaergen deposit was severely depleted in PGEs, possibly due to previous sulfide segregation at depth.

Supplementary Information The online version contains supplementary material available at https://doi.org/10.1007/s00126-021-01064-1.

Acknowledgements We thank Shoubo Chen, Zhaoming Zhao, and Xiwen Yin for assistant in the field work, and Yanguang Li, Shuangshuang Wang, and Yixiao Han for their analytical support. The manuscript was written during the first author's visit to Indiana University in 2020, which was financially supported by China Scholarship Council (grant No. 201908575010). Constructive comments from two anonymous reviewers and editorial guidance plus corrections from Wolfgang Maier and Bernd Lehmann are greatly appreciated.

Funding The study was financially supported by the National Science Foundation of China (Grant 41873053), China Geological Survey (DD20190143), the Second Tibetan Plateau Scientific Expedition and Research (STEP) (grants No. 2019QZKK0801 and No. 2019QZKK0806), and the Innovative Team of Magmatism Mineralization and Prospecting (grant No. 2020TD-030).

References

Amelin Y, Lee DC, Halliday AN, Pidgeon RT (1999) Nature of the Earth's earliest crust from hafnium isotopes in single detrital zircons. Nature 399:252–255

Arndt NT, Czamanske GK, Walker RJ, Chauvel C, Fedorenko VA (2003) Geochemistry and origin of the intrusive hosts of the Noril'sk-Talnakh Cu-Ni-PGE sulfide deposits. Econ Geol 98:495–515

Bai JK, Liu CY, Zhang SH, Lu JC, Sun JM (2018) Zircon U-Pb geochronology and geochemistry of basalts from the Qi'eshan group in the southern Turpan-Hami basin, East Tianshan: constraints on closure time of the North Tianshan Ocean. Acta Petrologica Sinica 34:2995–3010 ((**in Chinese with English abstract**))

Barnes SJ, Lightfoot PC (2005) Formation of magmatic nickel-copper-PGE sulfide deposits and processes affecting their copper and platinum group element contents. In Hedenquist, J.W., Thompson, J.F.H., Goldfarb, R.J., Richards, J.P., (eds.) Economic Geology 100th Anniversary Volume: 179–213

Barnes SJ, Mungall JE (2018) Blade-shaped dikes and nickel sulfide deposits: a model for the emplacement of ore-bearing small intrusions. Econ Geol 113:789–798

Blichert J, Albarède F (1997) The Lu-Hf isotope geochemistry of chondrites and the evolution of the mantle-crust system. Earth Planet Sci Lett 148:243–258

Campbell IH, Naldrett AJ (1979) The influence of silicate: sulfides ratios on the geochemistry of magmatic sulfides. Econ Geol 74:1503–1506

Chen YB, Hu AQ, Zhang GX, Zhang QF (2000) Precambrian basement age and characteristics of Southwestern Tianshan: zircon U-Pb geochronology and Nd-Sr isotopic compositions. Acta Petrologica Sinica 16:91–98 ((**in Chinese with English abstract**))

Corfu F, Hanchar JM, Hoskin PWO, Kinny P (2003) Atlas of zircon textures. Rev Mineral Geochem 53:469–500

Dare SAS, Barnes SJ, Prichard HM, Fisher PC (2010) The timing and formation of platinum-group minerals from the Creighton Ni-Cu-platinum-group element sulfide deposit, Sudbury, Canada: early crystallization of PGE-rich sulfarsenides. Econ Geol 105:1071–1096

DePaolo DJ, Wasserburg GJ (1979) Petrogenetic mixing models and Nd-Sr isotopic patterns. Geochim Cosmochim Acta 43:615–627

Ding X, Ripley EM, Li C (2012) PGE geochemistry of the Eagle Ni-Cu-(PGE) deposit, Upper Michigan: constraints on ore genesis in a dynamic magma conduit. Miner Deposita 47:89–104

Du AD, Wu SQ, Sun DZ, Wang SX, Qu WJ, Markey R, Stain H, Morgan J, Malinovskiy D (2004) Preparation and certification of Re-Os dating reference materials: molybdenites HLP and JDC. Geostand Geoanal Res 28:41–52

Fairchild LM, Swanson-Hysell NL, Ramezani J, Sprain CJ, Bowring SA (2017) The end of Midcontinent Rift magmatism and the paleogeography of Laurentia. Lithosphere 9:117–133

Han BF, Guo ZJ, He GQ (2010) Timing of major suture zones in North Xinjiang, China: constraints from stitching plutons. Acta Petrologica Sinica 26:2233–2246 ((**in Chinese with English abstract**))

Han YG, Zhao GC (2018) Final amalgamation of the Tianshan and Junggar orogenic collage in the southwestern Central Asian Orogenic Belt: constraints on the closure of the Paleo-Asian Ocean. Earth-Sci Rev 186:129–152

Hu AQ, Jahn BM, Zhang GX, Chen YB, Zhang QF (2000) Crustal evolution and Phanerozoic crustal growth in northern Xinjiang: Nd isotopic evidence. Part I. isotopic characterization of basement rocks. Tectonophysics 328:15–51

Irvine TN (1982) Terminology for layered intrusions. J Petrol 23:127–162

Jahn BM, Windley B, Natal'in B, Dobretsov N, (2004) Phanerozoic continental growth in Central Asia. J Asian Earth Sci 23:599–603

Jiao JG, Tang ZL, Qian ZZ, Sun T, Duan J, Jiang C (2012) Genesis and metallogenic process of Tulaergen large scale Cu-Ni sulfide deposit in eastern Tianshan area, Xinjiang. Acta Petrologica Sinica 28:3772–3786 ((**in Chinese with English abstract**))

Jiao JG, Zheng PP, Liu RP, Duan J, Jiang C (2013) SHRIMP zircon U-Pb age of the No. III intrusion in the Tulaergen Cu-Ni mining area, east Tianshan mountains, Xinjiang and its geological significance. Geology and Exploration 49:393–404 ((**in Chinese with English abstract**))

Keays RR, Lightfoot PC (2004) Formation of Ni-Cu-platinum group element sulfide mineralization in the Sudbury impact melt sheet. Mineral Petrol 82:217–258

Klemd R, John T, Scherer EE, Rondenay S, Gao J (2011) Changes in dip of subducted slabs at depth: petrological and geochronological evidence from H*P*-UH*P* rocks (Tianshan, NW China). Earth Planet Sci Lett 310:9–20

Koptev A, Calais E, Burov E, Leroy S, Gerya T (2018) Along-axis variations of rift width in a coupled lithospheremantle system, application to East Africa. Geophys Res Lett 45:5362–5370

Labidi J, Cartigny P, Moreira M (2013) Non-chondritic sulphur isotope composition of the terrestrial mantle. Nature 501:208–211

Lee CTA, Luffi P, Chin EJ, Bouchet R, Dasgupta R, Morton DM, Roux VL, Yin Q, Jin D (2012) Copper systematics in arc magmas and implications for crust-mantle differentiation. Science 336:64–68

Li C, Naldrett AJ (1999) Geology and petrology of the Voisey's Bay intrusion: reaction of olivine with sulfide and silicate liquids. Lithos 47:1–31

Li C, Naldrett AJ (2000) Melting reactions of gneissic inclusions with enclosing magma at Voisey's Bay, Labrador, Canada: implications with respect to ore genesis. Econ Geol 95:801–814

Li C, Barnes SJ, Makovicky E, Rose-Hansen J, Makovicky M (1996) Partitioning of nickel, copper, iridium, rhenium, platinum, and palladium between monosulfide solid solution and sulfide liquid:

effects of composition and temperature. Geochim Cosmochim Acta 60:1231–1238
Li C, Xu ZH, De Waal SA, Ripley EM, Maier WD (2004) Compositional variations of olivine from the Jinchuan Ni-Cu sulfide deposit, western China: implications for ore genesis. Miner Deposita 39:159–172
Li C, Arndt NT, Tang QY, Ripley EM (2015a) Trace element indiscrimination diagrams. Lithos 232:76–83
Li C, Zhang ZW, Li WY, Wang YL, Sun T, Ripley EM (2015b) Geochronology, petrology and Hf–S isotope geochemistry of the newly-discovered Xiarihamu magmatic Ni-Cu sulfide deposit in the Qinghai-Tibet plateau, western China. Lithos 216–217:224–240
Li C, Ripley EM, Tao Y (2019) Magmatic Ni-Cu and Pt-Pd sulfide deposits in China. Society of Economic Geologists Special Publications 22:483–508
Li JL, Gao J, Wang XH (2016) A subduction channel model for exhumation of oceanic-type high-pressure to ultrahigh-pressure eclogite-facies metamorphic rocks in SW Tianshan, China. Sci China Earth Sci 59:2339–2354
Li S, Wang T, Wilde SA, Tong Y, Hong DW, Guo QQ (2012a) Geochronology, petrogenesis and tectonic implications of Triassic granitoids from Beishan, NW China. Lithos 134–135:123–145
Li C, Thakurta J, Ripley EM (2012b) Low-Ca contents and kinkbanded textures are not unique to mantle olivine: evidence from the Duke island complex, Alaska. Mineral Petrol 104:147–153
Lightfoot PC, Naldrett AJ (1999) Geological and geochemical relationships in the Voisey's Bay intrusion Nain Plutonic Suite Labrador, Canada. Geological Association of Canada Short Course Notes 13:1–31
Liu HQ, Xu YG, Wei GJ, Wei JX, Yang F, Chen XY, Liu L, Wei X (2016) B isotopes of Carboniferous-Permian volcanic rocks in the Tuha basin mirror a transition from subduction to intraplate setting in Central Asian Orogenic Belt. Journal of Geophysical Research: Solid Earth 121:7946–7964
Liu XY, Wang Q (1995) Tectonics and evolution of the Beishan orogenic belt, West China. Geological Research 10:151–165
Lu SN, Li HK, Zhang CL, Niu GH (2008) Geological and geochronological evidence for the Precambrian evolution of the Tarim Craton and surrounding continental fragments. Precambr Res 160:94–107
Ludwig KR (2012) User's Manual for isoplot 3.75: a geochronological toolkit for Microsoft Excel. Berkeley Geochronological Center Special Publication 5: pp 75
Machado N, Simonetti A (2001) U-Pb dating and Hf isotopic composition of zircons by laser ablation-MC-ICP-MS. In: Sylvester P, ed. Laser-ablation-ICPMS in the Earth Sciences: principles and applications. Short Course, Mineral Assoc Can 29: 121–146
Mao QG, Xiao WJ, Windley BF, Han CM, Qu JF, Ao SJ, Zhang JE, Guo QQ (2012) The Liuyuan complex in the Beishan, NW China: a Carboniferous-Permian ophiolite fore-arc sliver in the southern Altaids. Geol Mag 149:483–506
Mao YJ, Qin KZ, Li C, Xue SC, Ripley EM (2014) Petrogenesis and ore genesis of the Permian Huangshanxi sulfide ore-bearing mafic-ultramafic intrusion in the Central Asian Orogenic Belt, western China. Lithos 200–201:111–125
Mao YJ, Qin KZ, Li C, Tang DM (2015) A modified genetic model for the Huangshandong magmatic sulfide deposit in the Central Asian Orogenic Belt, Xinjiang, western China. Miner Deposita 50:65–82
Marsh BD (2006) Dynamics of magmatic systems. Elements 2:287–292
Morgan WJ (1971) Convection plumes in the lower mantle. Nature 230:42–43
Mungall JE, Brenan JM (2014) Partitioning of platinum-group elements and Au between sulfide liquid and basalt and the origins of mantle crust fractionation of the chalcophile elements. Geochim Cosmochim Acta 125:265–289
Naldrett AJ (2011) Fundamentals of magmatic sulfide deposits. Rev Econ Geol 17:1–50
Naldrett AJ, Lightfoot PC, Fedorenko V, Doherty W, Gorbachev NS (1992) Geology and geochemistry of intrusions and flood basalts of the Noril'sk region, USSR, with implication for the origin of the Ni-Cu ores. Econ Geol 87:975–1004
Nie FJ, Jiang SH, Bai DM, Wang XL, Su XX, Li JC, Liu Y, Zhao XM (2002) Metallogenic studies and ore prospecting in the conjunction area of Inner Mongolia Autonomous region, Gansu Province and Xinjiang Uygur Autonomous Region (Beishan Mt), northwest China: Beijing, Geological Publishing House: pp 408 (in Chinese with English abstract).
Palme H, O'Neill HSC (2014) Cosmochemical estimates of mantle composition: Treatise on. Geochemistry 3:1–38
Pirajno F, Mao JW, Zhang ZC, Zhang ZH, Chai FM (2008) The association of mafic-ultramafic intrusions and A-type magmatism in the Tianshan and Altay orogens, NW China: implications for geodynamic evolution and potential for the discovery of new ore deposits. J Asian Earth Sci 32:165–183
Prichard HM, Knight RD, Fisher PC, McDonald I, Zhou MF, Wang CY (2013) Distribution of platinum-group elements in magmatic and altered ores in the Jinchuan intrusion, China: an example of selenium remobilization by post–magmatic fluids. Mineral Deposita 48:767–786
Qin KZ, Su BX, Sakyi PA, Tang DM, Li XH, Sun H, Xiao QH, Liu PP (2011) SIMS zircon U-Pb geochronology and Sr-Nd isotopes of Ni-Cu-bearing mafic-ultramafic intrusions in eastern Tianshan and Beishan in correlation with flood basalts in Tarim Basin (NW China): constraints on a ca. 280 Ma mantle plume. Am J Sci 311:237–260
Ripley EM, Li C (2011) A review of conduit related Ni-Cu-(PGE) sulfide mineralization at the Voisey's Bay deposit, Labrador, and the Eagle deposit, northern Michigan. Rev Econ Geol 17:181–198
Ripley EM, Li C (2013) Sulfide saturation in mafic magmas: is external sulfur required for magmatic Ni-Cu-(PGE) ore genesis? Econ Geol 106:45–58
Ripley EM, Brophy JG, Li C (2002) Copper solubility in a basaltic melt and sulfide liquid/silicate melt partition coefficients of Cu and Fe. Geochim Cosmochim Acta 66:2791–2800
Saktura WM, Buckman S, Nutman AP, Belousova EA, Yan Z, Aitchison JC (2017) Continental origin of the Gubaoquan eclogite and implications for evolution of the Beishan Orogen, Central Asian Orogenic Belt, NW China. Lithos 294–295:20–38
San JZ, Qin KZ, Tang ZL, Tang DM, Su BX, Sun H, Xiao QH, Liu PP (2010) Precise zircon U-Pb age dating of two mafic-ultramafic complexes at Tulaergen large Ni-Cu district and its geological implication. Acta Petrologica Sinica 26:3027–3035 ((**in Chinese with English abstract**))
Schmidberger SS, Francis D (1999) Nature of the mantle roots beneath the North American craton: mantle xenolith evidence from Somerset Island kimberlites. Developments in Geotectonics 24:195–216
Schmidt MW, Jagoutz O (2017) The global systematics of primitive arc melts. Geochem Geophys Geosyst 18:2817–2854
Shirey SB, Walker RJ (1998) The Re-Os isotope system in cosmochemistry and high-temperature geochemistry. Annu Rev Earth Planet Sci 26:423–500
Sláma J, Kosler J, Condon DJ, Crowley JL, Gerdes A, Hanchar JM, Horstwood MSA, Morris GA, Nasdala L, Norberg N, Schaltegger U, Schoene B, Tubrett MN, Whitehouse MJ (2008) Plesovice zircon-a new natural reference material for U-Pb and Hf isotopic microanalysis. Chem Geol 249:1–35
Soderlund U, Patchett JP, Vervoort JD, Isachsen CE (2004) The Lu-176 decay constant determined by Lu-Hf and U-Pb isotope systematics of Precambrian mafic intrusions. Earth Planet Sci Lett 219:311–324

Song X-Y, Chen L-M, Deng Y-F, Xie W (2013) Syncollisional tholeiitic magmatism induced by asthenosphere upwelling owing to slab detachment at the southern margin of the Central Asian Orogenic Belt. J Geol Soc 170:941–950

Song XY, Deng YF, Xie W, Yi JN, Fu B, Chen LM, Yu SY, Zheng WQ, Liang QL (2021) Prolonged basaltic magmatism and short-lived magmatic sulfide mineralization in orogenic belts. Lithos 390–391(6):106114

Studley SA, Ripley EM, Elswick ER, Dorais MJ, Fong J, Finkelstein D, Pratt LM (2002) Analysis of sulfides in whole rock matrices by elemental analyzer-continuous flow isotope ration mass spectrometry. Chem Geol 192:141–148

Su BX, Qin KZ, Zhou MF, Sakyi PA, Thakurta J, Tang DM, Liu PP, Xiao QH, Sun H (2014) Petrological, geochemical and geochronological constraints on the origin of the Xiadong Ural-Alaskan type complex in NW China and tectonic implication for the evolution of southern Central Asian Orogenic Belt. Lithos 200–221:226–240

Tang DM, Qin KZ, Sun H, Su BX, Xiao QH (2012) The role of crustal contamination in the formation of Ni-Cu sulfide deposits in eastern Tianshan, Xinjiang, northwest China: evidence from trace element geochemistry, Re-Os, Sr-Nd, zircon Hf-O, and sulfur isotopes. J Asian Earth Sci 49:145–160

Taranovic V, Ripley EM, Li C, Rossell D (2015) Petrogenesis of the Ni-Cu-PGE sulfide-bearing Tamarack intrusive complex, Midcontinent rift system, Minnesota. Lihtos 212–215:16–31

Taylor HPJr (1967) The zoned ultramafic complexes of southeastern Alaska. In: Wyllie, P. J. (ed.) Ultramafic and Related Rocks. John Wiley: pp 97–121

Thakurta J, Ripley EM, Li C (2008) Geochemical constraints on the origin of sulfide mineralization in the Duke Island Complex, southeastern Alaska. Geochem Geophys Geosyst 9:Q07003. https://doi.org/10.1029/2008GC001982

Tomkins AG, Rebryna KC, Weinberg RF, Schaefer BF (2012) Magmatic sulfide formation by reduction of Oxidized arc basalt. J Petrol 53:1537–1567

Wang F, Wei Z, Zhang G, Sun X (2004) New data of Silurian strata in areas of Hongshishan, north Beishan Mountains, Gansu Province of China. Geol Bull China 1123:1162–1163 ((**in Chinese with English abstract**))

Wang YH, Zhang FF, Liu JJ (2016) The genesis of the ores and intrusions at the Yuhai Cu-Mo deposit in eastern Tianshan, NW China: constraints from geology, geochronology, geochemistry, and Hf isotope systematics. Ore Geol Rev 77:312–331

Wang YH, Zhang FF, Li BC (2017) Genesis of the Yandong porphyry Cu deposit in eastern Tianshan, NW China: evidence from geology, fluid inclusions and isotope systematics. Ore Geol Rev 86:280–296

Wang YJ, Lv XB, Liu YR (2018) Petrogenesis and Ni-Cu-Co sulfide formation of mafic enclaves in Tulaergen mafic-ultramafic intrusive rocks, eastern Tianshan, northwest China: implications for liquid immiscibility and hydrothermal remobilization of platinum-group elements. Econ Geol 113:1795–1816

Wessel P, Kroenke LW (2009) Observations of geometry and ages constrain relative motion of Hawaii and Louisville plumes. Earth Planet Sci Lett 284:467–472

Wiedenbeck M, Alle P, Corfu F, Griffin WL, Meier M, Oberli F, Spiegel W (1995) Three natural zircon standards for U-Th-Pb, Lu-Hf, trace element and REE analyses. Geostand Geoanal Res 19:1–23

Woodland SJ, Pearson DG, Thirlwall MF (2002) A platinum group element and Re-Os isotope investigation of siderophile element recycling in subduction zones: composition of Grenada, Lesser Antilles arc, and the Izu-Bonin arc. J Petrol 43:171–198

Xiao WJ, Zhang LC, Qin KZ, Sun S, Li JL (2004) Paleozoic accretionary and collisional tectonics of the eastern Tianshan (China): implications for the continental growth of Central Asia. Am J Sci 304:370–395

Xiao WJ, Mao QG, Windley BF, Han CM, Qu JF, Zhang JE, Ao SJ, Guo QQ, Cleven NR, Lin SF, Shan YH, Li JL (2010) Paleozoic multiple accretionary and collisional processes of the Beishan Orogenic Collage. Am J Sci 310:1553–1594

Xiao WJ, Windley BF, Sun S, Li JL, Huang BC, Han CM, Yuan C, Sun M, Chen HL (2015) A tale of amalgamation of three collage systems in the Permian-Middle Triassic in Central Asia: oroclines, sutures and terminal accretion. Annu Rev Earth Planet Sci 43:477–507

Xiao WJ, Zheng YF, Hou ZQ, Windley BF, Zhao GC, Sun M, Zhang JE, Song DF, Zhang HR (2019) Tectonic framework and phanerozoic geologic evolution of China. SEG Special Publications 22:21–102

Xie W, Song XY, Deng YF, Wang YS, Ba DH, Zheng WQ, Li XB (2012) Geochemistry and petrogenetic implications of a late Devonian mafic-ultramafic intrusion at the southern margin of the Central Asian Orogenic Belt. Lithos 144–145:209–230

Xie W, Song XY, Chen LM, Deng YF, Zheng WQ, Wang YS, Ba DH, Yin MH, Luan Y (2014) Geochemistry insights on the genesis of the subduction-related Heishan magmatic Ni-Cu-(PGE) deposit, Gansu, northwestern China, at the southern margin of the Central Asian Orogenic Belt. Econ Geol 109:1563–1583

Xie W, Luo ZY, Xu YG, Chen YB, Hong LB, Ma L, Ma Q (2016) Petrogenesis and geochemistry of the late Carboniferous rear-arc (or back-arc) pillow basaltic lava in the Bogda Mountains, Chinese North Tianshan. Lithos 244:30–42

Xue SC, Li CS, Qin KZ, Tang DM (2016a) A non-plume model for the Permian protracted (266–286 Ma) basaltic magmatism in the Beishan-Tianshan region, Xinjiang, Western China. Lithos 256–257:243–249

Xue SC, Qin KZ, Li C, Tang DM, Mao YJ, Qi L, Ripley EM (2016b) Geochronological, petrological, and geochemical constraints on Ni-Cu sulfide mineralization in the Poyi ultramafic-troctolitic intrusion in the northeast rim of the Tarim Craton, western China. Econ Geol 111:1465–1484

Zhang CL, Zou H (2013) Comparison between the Permian mafic dykes in Tarim and the western part of Central Asian Orogenic Belt (CAOB), NW China: implications for two mantle domains of the Permian Tarim large igneous province. Lithos 174:15–27

Zhang X, Zhao G, Sun M, Eizenhöfer PR, Han Y, Hou W, Liu D, Wang B, Liu Q, Xu B (2016) Tectonic evolution from subduction to arc-continent collision of the Junggar ocean: constraints from U-Pb dating and Hf isotopes of detrital zircons from the North Tianshan belt, NW China. GSA Bull 128:644–600

Zhang YY, Yuan C, Long XP, Sun M, Huang ZY, Du L, Wang XY (2017) Carboniferous bimodal volcanic rocks in the Eastern Tianshan, NW China: evidence for arc rifting. Gondwana Res 43:92–106

Zhao GC, Cawood PA (2012) Precambrian geology of China. Precambr Res 222–223:13–54

Zhao Y, Xue CJ, Liu SA, Symons DTA, Zhao XB, Yang YQ, Ke JJ (2017) Copper isotope fractionation during sulfide-magma differentiation in the Tulaergen magmatic Ni-Cu deposit, NW China. Lithos 286–287:206–215

Zhou TF, Yuan F, Zhang DY, Fan Y, Liu S, Peng MX, Zhang JZ (2010) Geochronology, tectonic setting and mineralization of granitoids in Jueluotage area, eastern Tianshan, Xinjiang. Acta Petrologica Sinica 26:478–502 ((**in Chinese with English abstract**))

Zuo GC, Zhang SL, He GQ, Zhang Y (1990) Early Paleozoic plate tectonics in Beishan area. Sci Geol Sin 4:305–314

Zuo GC, Zhang SL, He GQ, Zhang Y (1991) Plate tectonic characteristics during the early Paleozoic in Beishan near the Sino-Mongolian border region, China. Tectonophysics 188:385–392